NUMERICAL SIMULATION OF CORROSIVE DISSOLUTION AND STRESS-INDUCED CHANGES IN THE REACTION RATES

A Dissertation

Presented to the Faculty of the Graduate School

of Cornell University

in Partial Fulfillment of the Requirements for the Degree of

Doctor of Philosophy

by

Swarnavo Sarkar

January 2013

© 2013 Swarnavo Sarkar
ALL RIGHTS RESERVED

NUMERICAL SIMULATION OF CORROSIVE DISSOLUTION AND STRESS-INDUCED CHANGES IN THE REACTION RATES

Swarnavo Sarkar, Ph.D.

Cornell University 2013

This dissertation is composed of three chapters. Each chapter addresses a specific topic and has been, or will be, submitted as a journal article. The overarching theme connecting the content of the three chapters is the problem of accurately determining the rate off corrosion in alloy-electrolyte systems. At the beginning of every chapter there is a separate abstract that has been prepared for the respective journal publication.

Broadly, in order to computationally simulate the process of corrosion we need the following: a knowledge of the physical laws that govern the rate of corrosion, a framework to compute the rate for alloy-electrolyte systems using these laws, and a method to update the position and the electrochemical properties of a corrosive front using the computed reaction rate. In the electrolytic domain, the effect of ionic concentration on the reaction rate is computed using ionic transport models. The most commonly used ionic transport model combines a set of Nernst-Planck equations with the electroneutrality condition without including the Gauss' law. On the other hand, the methods using Gauss' law have been reported to be challenging for a numerical solution. We developed an alternative ionic transport model based on Onsager's theory of near-equilibrium dissipative processes. We assumed the flow caused due to ionic interactions, as obtained using Onsager's theory, to be an additional unknown for the ionic transport model. We proposed that the flux density created due to

this additional flow is the minimum that is required to satisfy the electroneutrality condition. Using our method we were able to reproduce the transient characteristics of electrodes that agreed in behavior with experimental observations. Also based on our numerical simulations, we observed that the dissipation due to ionic interactions is higher near the ionic sources at the boundaries and diminishes gradually into the bulk of the electrolyte.

The motion of an alloy-electrolyte interface due to corrosion is a multiscale problem in time. The ionic transport process evolves at a time step depending on the diffusivity of the ions and dimensions of the anodic-cathodic regions on an alloy surface. It turns out that this time step is several order of magnitudes smaller than the time step at which we can observe a significant change in the alloy-electrolyte boundary due to corrosion. We proposed a quasi-steady state assumption in order to alleviate this problem. We assumed that for a fixed description of the alloy-electrolyte boundary there exists a steady state solution to the corrosion current density as dictated by the ionic transport process. This is a reasonable assumption for several corrosive systems, particularly for the ones surrounded by seawater. A finite element framework with adaptive remeshing was developed that uses the ionic transport model described above to determine the corrosion rate and explicitly integrate the motion of the corrosive front. We studied and observed the convergence of this method with respect to refinement in time steps. This framework was built to modify the electrodic properties along an alloy-electrolyte interface depending upon the material composition of the alloy domain. Using this methodology we can computationally determine the evolution of the anode-cathode ratio and the corrosion current density for given organization of anodic and cathodic phases within an alloy domain.

Most of the alloy structures that suffer corrosion are designed to transfer mechanical load. Hence, it is important to understand the impact of a stress field on the reaction kinetics that has been experimentally measured for an unstressed alloy. We used a stress-dependent chemical potential from the Gibbs-Duhem equation and used it to derive the reaction kinetics along the lines of the well-established Butler-Volmer model. In the presence of a stress field our model introduces an additional amplification-reduction factor to the forward and the reverse components of the Butler-Volmer kinetics. We further explored that the mechanical-electrochemical coupling produces a change in the shape of a dissolution front in addition to the change in the reaction rate. In our study we also examined the possible change in the reaction rate due stress-induced surface instabilities. Our calculations show that the combined shift in the reaction rate due to stress and surface patterns can be quite different from the change obtained due to the same stress field in the absence of patterns.

BIOGRAPHICAL SKETCH

Swarnavo grew up in Kolkata, India. After completing high school, he joined Indian Institute Technology at Kharagpur to pursue undergraduate studies in Civil Engineering. At the end of his junior year at college he spent his summer as an intern at GE Global Research, Bangalore, where he performed fatigue analysis of wind turbine bedplates and learnt using finite element software at a professional level. He graduated from IIT on Spring 2007, and spent the following summer studying the bending of carbon nanotubes using molecular dynamics simulation under the guidance of Professor Baidurya Bhattacharya.

On Fall 2007, Swarnavo joined Cornell University as a graduate student in Civil and Environmental Engineering. His graduate research work under the advisement of Dr. Wilkins Aquino can divided into two parts: developing computational tools to simulate progressive damage due to corrosion, and understanding the influence of mechanical-electrochemical interaction on the corrosion kinetics. His graduate coursework has covered the disciplines of continuum mechanics, computational science, and mathematical analysis. He continued his research at Cornell University until the end of 2011, before relocating along with his research group to Duke University on Spring 2012.

To my family.

ACKNOWLEDGEMENTS

It is difficult to commensurate the guidance of my thesis advisor Dr. Wilkins Aquino using a few words of gratitude. I have been fortunate to pursue a unique and interdisciplinary research direction under him, and profited with a thorough background in the finite element method through his classes. In particular, I appreciate his advice towards balancing the technical depth of a problem with a broad research vision. My research work would not have been possible without his support.

I am thankful to Dr. Derek Warner for our discussions and for the memorable experience that I have gained as a teaching assistant in his class. I would like to thank Professor Lars Wahlbin for his insightful suggestions about my work, about technical writing, and for his course on partial differential equations, which included many interesting problems. I am also grateful to Professor Leonard Gross whose classes form a major part of my graduate training.

Much appreciation is due to my fellow research group members, Manuel Diaz, Gabriel De Frias, and my triathlon teammates, Anthony Sabelli and Jim Warner. A special mention will go to Jim for our research collaboration. I acknowledge my friend Anirban Ghosh at John Hopkins University with whom I have spent hours discussing thermodynamics. I also extend my thanks to my friends and fellow graduate students at Cornell, especially to Saifur Rahman and Saba Khan.

Finally, I am grateful for the unwavering support that I have received over the years from my parents and my brother.

TABLE OF CONTENTS

LIST OF TABLES

LIST OF FIGURES

CHAPTER 1

ELECTRONEUTRALITY AND IONIC INTERACTIONS IN THE MODELING OF MASS TRANSPORT IN DILUTE ELECTROCHEMICAL SYSTEMS

We propose a simple, but novel mathematical and numerical approach to describe mass transport in dilute solutions, taking into consideration ionic interactions. Our proposed approach treats fluxes due to ionic interactions as additional unknowns in the transport equation. Through variational arguments, we derive a simple expression for these ionic fluxes in terms of the electroneutrality condition, which allows for a straightforward treatment of the new unknowns. Furthermore, a finite element formulation based on our mathematical model is presented. Finally, using the distribution of the interionic flux density and an energy dissipation function, we show that besides properly capturing flow due to ionic interactions, our model can also describe independent ionic flow as predicted by the conventional Nernst-Planck equation in regions where ionic interactions are weak.

1.1 Introduction

The need to model dilute electrochemical systems arises across a diverse spectrum of engineering and science applications such as simulating the corrosion of alloys, the kinetics of fuel cells, etc. The elementary constituents of an electrochemical system are ions, and in a many real applications the population of ions is high enough to seek a description at the continuum level. Based on the

S. Sarkar and Wilkins Aquino, Electroneutrality and ionic interactions in the modeling of mass transport in dilute electrochemical systems, Electrochimica Acta 56, no. 24 (2011), 8969-8978.

principle of conservation of mass, the Nernst-Planck equation [21] is used to describe the transport of an ionic distribution due to diffusion, migration, and convection. The migration term is present due to the flow of ions in the electric potential field present in the electrochemical domain. Although the electric potential field is only an input to the Nernst-Planck equation, the field itself is determined by the distribution of all the ions in the domain using Gauss' law.

A common approach to model dilute electrochemical systems is to solve the Nernst-Planck equation and Gauss' law as a coupled system. However, attempts to obtain numerical solutions to this coupled system of equations have encountered difficulty due to numerical stiffness [16, 8]. In practice, several approaches have been proposed to alleviate this challenge. For example, in order to simplify the governing equations, a quasi-potential transformation was proposed under the assumption that the concentration fields are single-valued functions of the electric potential field [20].

Another, and perhaps the most prevalent, approach to model ionic distribution is based on the assumption that the electrostatic interactions between ions cause the electrolyte to have a net zero charge density, yielding the electroneutrality condition. Hence, it is common to use the Nernst-Planck equation coupled with the electroneutrality condition to describe an electrochemical system [25, 3, 10]. However, this approach ignores Gauss' law in a domain consisting of charged particles and produces a potential field that does not satisfy the fundamental physics described by Gauss' law. There are, however, few works that have reported solutions to the original system of equations [9](*i.e.* the Nernst-Planck equation with Gauss' law). It is important to keep in mind that the Nernst-Planck equation, in its basic form, ignores transport due ionic

interaction.

While conservation of mass is an obvious approach to derive the ionic transport equation, Onsager's work[17] in 1931 presented a generalized formulation for dissipative thermodynamic systems which can be used to model ionic transport. According to this formalism, the total flux for an ion is given as the linear combination of all the thermodynamic forces present in an electrochemical system. According to Onsager's formulation, the Nernst-Planck equation neglects the cross-coefficients that represent ioinic interactions in the definition of mass transport [19]. It has been observed in experiments that these coefficients can be significant in comparison to the chemical drag coefficient [15] . Also, neglecting these cross-coefficients hampers the applicability of the Nernst-Planck equation in ion-exchanger membranes and multi-ionic solutions, among others [2].

In this paper, we propose an approach to consider ionic interactions in the modeling of electrochemical systems. The independent flow hypothesis, that results by neglecting the cross-coefficients in Onsager's formulation, assumes that the ionic distribution are evolving independently of each other. In the Background section, we review a common methodology for modeling electrochemical systems and analyze its consistency with the independent flow assumption. Then, we propose a novel and simple method that takes into consideration ionic interactions through a constrained variational principle. Our resultant formulation uses the Nernst-Planck equation, the electroneutrality condition, and Gauss' law. In addition, we also present a finite element formulation to obtain numerical approximations of the proposed mathematical model. Finally, we show some numerical results that verify the convergence and stability of our finite element formulation and the physico-chemical consistency of the proposed

mathematical model.

1.2 Background

In this section, we present the governing equations that are commonly used to describe a dilute electrochemical system. We discuss the assumptions made about the Coulombic interactions between ions and observe the effect of these assumptions on the governing equations.

Let an electrolytic region in space can be represented as Ω_E. We assume this region to contain n ionic species. Hence, the field variables in Ω_E are n concentration fields, and an electric potential field. We represent the concentration fields as c_i, where $i = 1, \ldots, n$, and the electric potential field as φ. These fields are functions of space and time, but we suppress their dependence for simplicity in the notation. Corresponding to each ion, a chemical potential field can be defined as

$$\mu_i = z_i F \varphi + RT \log c_i \quad \forall \quad i = 1, \ldots, n \tag{1.1}$$

where z_i is the charge of the ion, F is the Faraday's constant, R is the gas constant, and T is the temperature. In electrolytes, ionic motion is driven by thermodynamic forces, $\vec{X}_i$, which are negative gradients of the chemical potentials and are given as

$$\vec{X}_i = -\nabla \mu_i \quad \forall \quad i = 1, \ldots, n \tag{1.2}$$

According to Onsager[17], the flux for an ion, $\vec{J}_i$, can be represented as a linear combination of the thermodynamic forces

$$\vec{J}_i = \sum_{k=1}^{n} L_{ik} \vec{X}_k \tag{1.3}$$

where $L_{ii} = \frac{D_i}{RT} c_i$, with D_i being the diffusion coefficient for ion i. For $i \neq k$, $L_{ik} = L_{ki}$, as dictated by Onsager's reciprocal relations. The coefficient $L_{ik}, i \neq k$ represents the drag on chemical species i due to the thermodynamic force from ion k. The values for these coefficients are not as easily available as the diffusion coefficients [2]. It may be possible to construct a computational model to calculate these macroscopic quantities by simulating the particle to particle interactions for a large number of particles. However, this approach would be very computationally expensive and infeasible for practical problems. In our work, we resort to the phenomenological observation that electroneutrality is a consequence of Coulombic interactions in order to approximate the effect of the cross-coefficients L_{ik}, $i \neq k$.

Using the expression for the flux shown in (2.3), we can formulate the transport equation for ion i as

$$\frac{\partial c_i}{\partial t} = -\nabla \cdot \vec{J_i} + q_i - \nabla \cdot (c_i \vec{v}) \quad \text{in} \quad \Omega_E \tag{1.4}$$

where q_i is the source/sink term due to chemical reactions. The last term represents flux density due to the velocity field $\vec{v}$. Since

$$L_{ii} \vec{X_i} = -D_i \nabla c_i - \frac{z_i F}{RT} (D_i c_i \nabla \varphi) \tag{1.5}$$

we split the flux term $\vec{J_i}$ into contributions from the independent motion of ion i and the interaction of this ion with other ions as

$$\vec{J_i} = -D_i \nabla c_i - \frac{z_i F}{RT} (D_i c_i \nabla \varphi) - \sum_{k=1, k \neq i}^{n} L_{ik} \nabla \mu_k \tag{1.6}$$

Substituting the expression for flux from Equation (1.6) into Equation (2.4), we obtain

$$\frac{\partial c_i}{\partial t} = \nabla \cdot (D_i \nabla c_i) + \frac{z_i F}{RT} \nabla \cdot (D_i c_i \nabla \varphi) + \nabla \cdot \left(\sum_{k=1, k \neq i}^{n} L_{ik} \nabla \mu_k \right) + q_i - \nabla \cdot (c_i \vec{v}) \tag{1.7}$$

Equation (1.7) is the basis for our proposed development as it describes ionic transport in the most general case. By general, we mean an electrochemical model where ionic interactions are in effect. Interactions between ions will always exist. As stated by Onsager[19], if the reciprocal coefficients, $L_{ik}(i \neq k)$, are neglected, the ions in an electrolyte are assumed to move independently, which means that at any instant in time the concentration fields, c_i, are independent of each other. Hence, the assumption of independent flow reduces equation (1.7) to the usual Nernst-Planck equation

$$\frac{\partial c_i}{\partial t} = \nabla \cdot (D_i \nabla c_i) + \frac{z_i F}{RT} \nabla \cdot (D_i c_i \nabla \varphi) + q_i - \nabla \cdot (c_i \vec{v}) \tag{1.8}$$

We emphasize that both the equations (1.7) and (1.8) describe ionic transport, but they differ by the assumption of ions flowing independently.

Since an electrochemical domain consists of charged particles (ions), the second governing equation needed to describe our electrochemical system is Gauss' law, which is mathematically expressed as

$$\nabla^2 \varphi = -\frac{F}{\varepsilon} \sum_{i=1}^{n} z_i c_i \quad \text{in} \quad \Omega_E \tag{1.9}$$

where ε is the permittivity of the electrolytic medium. Gauss' law describes the nature of the electric potential field generated due to Coulombic interactions, and Coulombic forces affect the migration velocities of ions [18]. Let the concentration field for ion k, c_k, be perturbed while keeping the other ionic distributions unchanged. Then, from Equation (1.9), a change in the gradient of electric potential, $\nabla \varphi$, is evident. Since $\nabla \varphi$ is causing the drift of all the ions($i = 1, \ldots, n$), we can conclude that the change in the distribution of any one of the ions is also affecting the flow of the rest of the ions. Hence, by enforcing Equation (1.9) we would violate the assumption of independently flowing ions behind Equation (1.8).

One could state that information about ionic interactions is present in Equation (1.8) through the electric potential, φ. However, notice that at any given time, Equation (1.9) defines an electric potential field arising from the ionic distribution at this time. But, Equation (1.8) describes the independent motion of ion i in this potential field and ignores the changes that occur in φ due to the motion of other ions. That is, Equation (1.8) lacks information about ionic interactions. Therefore, we may have a solution to Equation (1.8) after obtaining a solution of Equation (1.9)(or fixing the electric potential field), but not a solution to both of them simultaneously, unless ionic interactions are negligible.

The previous paragraph explains the differences in the assumptions behind Equations (1.8) and (1.9). We will now briefly survey the current approaches for solving these equations numerically. It has been widely reported in the literature[16, 8, 20, 25] that discretization of equations (1.8) and (1.9) yield linear (or nonlinear, depending on the boundary conditions and source term) systems that are difficult to solve. This numerical difficulty arises due to the magnitude of the factor $\frac{F}{\varepsilon}$(around 10^{14} for water in SI units). The factor $\frac{F}{\varepsilon}$ causes numerically large potential gradients, $\nabla\varphi$, for small values of the $\sum z_i c_i$. Despite this numerical difficulty, it is possible to use numerical scaling techniques to obtain approximate solutions to this stiff system. Keeping these issues in mind, we reiterate that Equations (1.8) and (1.9) are based on assumptions that are not in accordance with each other, unless ionic interactions are weak.

Another common macroscopic approximation about an ionic solution is electroneutrality [16], which is mathematically expressed as

$$\sum_{i=1}^{n} z_i c_i = 0 \quad \text{in} \quad \Omega_E \tag{1.10}$$

Electroneutrality means that the net charge density in an ionic solution is zero.

Unlike equations (1.7), (1.8), and (1.9), electroneutrality is not a governing equation for an electrochemical domain. It is a consequence of Coulombic interactions. If the net charge density is not zero, it causes high potential gradients that redistribute the ions to render the solution almost electrically neutral.

A popular method for modeling dilute ionic solutions consists of numerically solving Equation (1.8) simulataneously with Equation (2.5). The basic premise for this method is that equations (1.8) and (2.5) form a set of $n + 1$ equations from which we can obtain n concentration fields, and the electric potential field. Since the right hand side of Equation (1.9) is separately satisfied to be zero by Equation (2.5). The resulting electric potential field, φ, is expected to satisfy Gauss' law in homogeneous form as

$$\nabla^2 \varphi = 0 \quad \text{in} \quad \Omega_E \tag{1.11}$$

However, the field distribution φ, obtained from equations (1.8) and (2.5) does not satisfy Equation (1.11). Moreover, we cannot derive Gauss' law from Equations (1.8)) and (2.5). We make two more statements regarding the compatibility of Equations (1.8) with (2.5). First, as electroneutrality is a consequence of Coulombic interactions, the solution to Equations (1.8) and (2.5) should satisfy Equation (1.9) or (1.11), which describes Coulombic interactions for concentration fields. Second, Equation (1.8) assumes the flow of independent distributions, but Equation (2.5) violates this assumption by stating the concentration fields to be linearly dependent.

In summary, the set of equations that can adequately describe ionic transport with Coulombic interactions are equations (1.7) and (1.9), both of which consider ionic interactions. However, the reciprocal coefficients that define ionic interactions, are not as easily available as the diffusion coefficients. So, solving

these equations is not possible unless L_{ik} are available. In the approach proposed in this work, the electroneutrality condition (2.5) is used as a way to describe ionic interactions. Then, the general transport equation (1.7) can be used with the homogeneous Gauss' law (1.11) to derive a consistent set of equations.

1.3 Formulation

1.3.1 Consistent set of equations

The objective of this section is to formulate a consistent set of equations(*i.e.* taking ionic interactions into consideration) to model dilute ionic solutions. First, we develop a formulation for general ionic transport(*i.e.* with interactions) using a variational principle, and then show that it reduces to the ideal ionic transport(one without interactions) in the absence of any additional conditions (*e.g.* electroneutrality) on the ionic distributions. Then, we include in this formulation the constraint of electroneutrality, which circumvents the need to specify the cross coefficients in the transport equation. Also, in this section we omit any contribution due to convection in ionic transport for the sake of brevity. However, our formulation is also applicable to the case of convective ionic transport.

As explained in the previous section, Equation (1.7) governs the ionic transport in a general case. However, the cross coefficients, $L_{ik}, i \neq k$, are difficult to obtain [2]. To circumvent this difficulty, we propose that for a given ion i, we condense the contribution of all the cross-coefficients to the flux density $\nabla \cdot \vec{J_i}$ into an additional unknown. We refer to this additional unknown as r_i, which

is defined as

$$r_i = \nabla \cdot \left(\sum_{k=1, k \neq i}^{n} L_{ik} \nabla \mu_k \right) \tag{1.12}$$

Then, substituting Equation (1.12) into Equation (1.7) we obtain

$$\frac{\partial c_i}{\partial t} = \nabla \cdot (D_i \nabla c_i) + \frac{z_i F}{RT} \nabla \cdot (D_i c_i \nabla \varphi) + q_i + r_i \tag{1.13}$$

The term r_i can be interpreted as the rate of accumulation of ion i at a point in Ω_E due to ionic interactions. We will refer to r_i as the interionic flux density. It is important to notice that Equation (1.13) represents the independent motion of ions when $r_i = 0$ as in the classical Nernst-Planck equation (1.8). Hence, we can consider r_i as an additional variable in Equation (1.13), which controls the extent of interactions between ions. If $r_i = 0$, then interactions are absent.

For a dilute ionic system with n ions, we have n additional variables r_i. In the case of independent flow, we know that these variables are zero. When Coulombic interactions are considered in the description of ionic motion, then we have an additional phenomenological statement in the electroneutrality condition. The electroneutrality condition makes the concentration fields dependent upon each other, and we need to determine the additional variables r_i using (2.5).

Since we need to determine n variables from one condition(*i.e.* electroneutrality) (2.5), and we know that these variables r_i become zero in the absence of this condition, we propose the following. In a dilute ionic system, the additional variables r_i are determined by minimizing their magnitude subject to the constraint of electroneutrality. The latter can be accomplished by formulating a constrained functional optimization problem [13]. To this end, we proceed by defining a measure of the magnitude of the interionic fluxes over the domain as

$$\mathbb{J}(r_1, \ldots, r_n) = \frac{1}{2} \sum_{i=1}^{n} \int_{\Omega_E} r_i^2 \, d\Omega \tag{1.14}$$

The goal is to find the values of the interionic fluxes, r_i, that minimize the above functional subject to the condition of electroneutrality. This goal can be achieved by solving the following constrained minimization problem

$$\begin{aligned} &\text{minimize } \mathbb{J}(r_1, \ldots, r_n) \\ &\text{subject to } g = 0 \end{aligned} \tag{1.15}$$

The above problem can be solved by finding the stationary points of the following functional [13]

$$\mathbb{W}(r_1, \ldots, r_n, \lambda) = \mathbb{J}(r_1, \ldots, r_n) + \int_{\Omega_E} \lambda g \, d\Omega \tag{1.16}$$

where λ is the Lagrange multiplier, and g is the constraint that needs to be satisfied by r_i, which in our case is electroneutrality. The stationary points of $\mathbb{W}$ represent the smallest magnitudes of r_i that satisfy electroneutrality. In order to find the stationary points for $\mathbb{W}$, we need to compute its Gâteaux derivative [13, 22], which is defined as

$$\langle D\mathbb{W}(u), h\rangle = \frac{d}{d\epsilon}\mathbb{W}(u + \epsilon h)\bigg|_{\epsilon=0} \tag{1.17}$$

where u is one of the variables(*i.e.* r_i or λ) of the functional $\mathbb{W}$. At the stationary points of $\mathbb{W}$, the Gâteaux derivative $\langle D\mathbb{W}(u), h\rangle$ is zero for all h.

It is instructive to realize that the constraint function g would be absent if there are were interactions between the ions and they were flowing independently. In that case, the variables r_i are determined by minimizing the unconstrained functional $\mathbb{W}$, which is

$$\mathbb{W}(r_1, \ldots, r_n) = \frac{1}{2}\int_{\Omega_E} \sum_{i=1}^{n} r_i^2 \, d\Omega \tag{1.18}$$

and its Gâteaux derivative with respect to r_j is

$$\langle D\mathbb{W}(r_j), h\rangle = \int_{\Omega_E} r_j h \, d\Omega \tag{1.19}$$

which is zero for all h if and only if $r_j = 0$. Hence, Equation (1.13) reduces to Equation (1.8) when the ionic distributions are assumed to be independent of each other.

Now we will derive the mathematical form of r_i that arises from electroneutrality. Taking the time derivative of the electroneutrality condition leads to

$$\sum_{i=1}^{n} z_i \dot{c}_i = 0 \tag{1.20}$$

Additionally, we define a quantity ρ_I as

$$\rho_I = \sum_{i=1}^{n} z_i \left(\nabla \cdot (D_i \nabla c_i) + \frac{z_i F}{RT} \nabla \cdot (D_i c_i \nabla \varphi) \right) \tag{1.21}$$

which is the rate of accumulation of charge at a point in Ω_E due to independent flow of all the ions.

Multiplying Equation (1.13) by z_i and summing over all the ions, we obtain

$$\sum_{i=1}^{n} z_i \dot{c}_i = \rho_I + \sum_{i=1}^{n} z_i r_i \tag{1.22}$$

The generation and loss terms, q_i, vanish from Equation (1.22) because we have assumed that the net charge produced by the chemical reactions in the bulk of the system is zero. Hence, we can write

$$\rho_I + \sum_{i=1}^{n} z_i r_i = 0 \tag{1.23}$$

as a condition on r_i due to electroneutrality. So, we have translated a constraint on the concentration fields to a constraint on the variables r_i. Using Equation (1.23), we define the constraint function g as

$$g(r_1, \ldots, r_n) = \rho_I + \sum_{i=1}^{n} z_i r_i \tag{1.24}$$

Consequently, the constrained functional is given now as

$$\mathbb{W}(r_1, \ldots, r_n, \lambda) = \frac{1}{2} \int_{\Omega_E} \sum_{i=1}^{n} r_i^2 \, d\Omega + \int_{\Omega_E} \lambda(\rho_I + \sum_{i=1}^{n} z_i r_i) \, d\Omega \tag{1.25}$$

The Gâteaux derivative of $\mathbb{W}$ with respect to r_j is

$$\langle D\mathbb{W}(r_j), h \rangle = \int_{\Omega_E} (r_j + z_j \lambda) h \, d\Omega \tag{1.26}$$

Setting the above derivative (1.26) to zero for all h, we obtain the condition $r_j = -z_j \lambda$. Substituting this result in Equation (1.13), we get

$$\frac{\partial c_i}{\partial t} = \nabla \cdot (D_i \nabla c_i) + \frac{z_i F}{RT} \nabla \cdot (D_i c_i \nabla \varphi) + q_i - z_i \lambda \tag{1.27}$$

Also, the Gâteaux derivative of $\mathbb{W}$ with respect to λ is

$$\langle D\mathbb{W}(\lambda), h \rangle = \int_{\Omega_E} (\rho_I + \sum_{i=1}^{n} z_i r_i) h \, d\Omega \tag{1.28}$$

So, setting Equation (1.28) to zero leads to Equation (1.23), which we have developed from the electroneutrality condition (2.5).

In the end, we obtain n equations given by (1.27), one for each ion, describing the ionic flow constrained by the electroneutrality condition (2.5). Equations (1.27) and (2.5) define a system of $n + 1$ equations with $n + 1$ unknowns (*i.e.* n concentration fields, and a Lagrange multiplier field). It is important to realize that the Lagrange multiplier field describes the flux density due to ionic interactions. Notice that the field λ is common to all the ions. The fact that we end up with one field for all the ions results from incorporating one additional equation(*i.e.* electroneutrality) in describing our electrochemical model. That is, we can compute only one extra field variable in addition to the concentrations and the electrostatic potential. Furthermore, notice that the effect of electroneutrality on the ionic flux appears in our formulation in an integral sense (*i.e.* minimization of a functional), which lumps this effect into the additional unknown λ.

The electric potential field has to be determined using Gauss' law. Since we are satisfying electroneutrality explicitly, the right hand side of Equation (1.9) vanishes. So, we use Gauss' law in its homogeneous form as

$$\nabla^2 \varphi = 0 \tag{1.29}$$

In summary, our proposed mathematical model consists of equations (1.27), (2.5), and (1.29) plus appropriate boundary and initial conditions. The main assumptions behind these equations are that interactions of only Coulombic nature exist between the ions, and that these interactions cause the minimum deviation from the independent flow (1.5) of ions. The background section motivated the need to consider ionic transport, electroneutrality, and Gauss' law simultaneously to describe dilute ionic systems, and this subsection showed a way to achieve it. In the following subsection, we present a Finite Element scheme to approximate the solution of Equations (1.27), (2.5), and (1.29).

1.3.2 Finite Element formulation

We will first derive the weak formulation [5] of the coupled governing equations. Weak solutions, c_i and φ, to the system of equations (1.27), (2.5), and (1.29) belong to the space $H^1(\Omega_E)$[6], which consists of functions that along with their first weak derivative are square integrable. Since there are no derivatives for the Lagrange multiplier in Equation (1.27), we take $\lambda \in L^2(\Omega_E)$[1], which is the space of square integrable functions. The system of equations (1.27), (2.5), and (1.29) are applicable inside the domain Ω_E. At the boundaries, we need to specify flux/current(*i.e.* Neumann) boundary conditions, or concentration/potential(*i.e.* Dirichlet) boundary conditions in order to obtain particular

solutions for an electrochemical system [23]. We split Γ_E, the boundary of the domain Ω_E, into two parts Γ_D and Γ_N such that $\Gamma_D \cup \Gamma_N = \Gamma_E$ and $\Gamma_D \cap \Gamma_N = \varnothing$. Γ_D denotes the part of the domain where Dirichlet boundary conditions are specified, and Γ_N denotes the part of the boundary where Neumann boundary conditions are prescribed. We specify the Dirichlet boundary conditions (concentration values) as

$$c_i = u_i \quad \text{on} \quad \Gamma_D \tag{1.30}$$

and the Neumann boundary conditions(concentration flux) as

$$-\frac{z_i D_i F}{RT} c_i \nabla\varphi \cdot \vec{n} - D_i \nabla c_i \cdot \vec{n} = f \quad \text{on} \quad \Gamma_N \tag{1.31}$$

where $\vec{n}$ is the unit outward normal vector on the boundary Γ_N. Let $w \in H^1(\Omega_E)$ such that $w = 0$ over Γ_D. Multiplying Equation (1.27) by w and using Gauss' divergence theorem [7], we obtain the weak form of the general transport equation as

$$\begin{aligned}\int_{\Omega_E} w\dot{c_j} d\Omega =& \frac{z_i F}{RT} \int_{\Gamma_D} w D_i c_i \nabla\varphi \cdot \vec{n}\, d\Gamma + \int_{\Gamma_D} w D_i \nabla c_i \cdot \vec{n}\, d\Gamma + \frac{z_i F}{RT} \int_{\Gamma_N} w D_i c_i \nabla\varphi \cdot \vec{n}\, d\Gamma \\ &+ \int_{\Gamma_N} w D_i \nabla c_i \cdot \vec{n}\, d\Gamma - \frac{z_i F}{RT} \int_{\Omega_E} \nabla w \cdot (D_i c_i \nabla\varphi)\, d\Omega - \int_{\Omega_E} \nabla w \cdot (D_i \nabla c_i)\, d\Omega \\ &+ \int_{\Omega_E} w q_i\, d\Omega - \int_{\Omega_E} w z_i \lambda\, d\Omega \end{aligned} \tag{1.32}$$

Gauss' divergence theorem is given as

$$\int_{\Omega_E} \nabla \cdot \vec{u}\, d\Omega = \int_{\Gamma_E} \vec{u} \cdot \vec{n}\, d\Gamma_E \tag{1.33}$$

where $\vec{u}$ is a continuous differentiable vector field over the domain Ω_E.

The first two boundary integrals over Γ_D in Equation (2.20) vanish because $w = 0$ over Γ_D. Substituting Equation (1.31) in the third and the fourth boundary

integrals over Γ_N, we get

$$\int_{\Omega_E} w\dot{c_j} d\Omega = -\int_{\Gamma_N} wf\, d\Gamma - \frac{z_i F}{RT}\int_{\Omega_E} \nabla w \cdot (D_i c_i \nabla\varphi)\, d\Omega - \int_{\Omega_E} \nabla w \cdot (D_i \nabla c_i)\, d\Omega + \int_{\Omega_E} wq_i\, d\Omega - \int_{\Omega_E} wz_i\lambda\, d\Omega \tag{1.34}$$

In the Finite Element Method, the approximation for the scalar field c_i is given as $c_i^h(\vec{x},t) = [N(\vec{x})]\{c_i(t)\}$ [24]. Where $[N(\vec{x})]$ is the interpolation matrix, and $\{c_i(t)\}$ is the vector consisting of the field values at the nodes of a finite element mesh for ion *i*. Similarly, the electric potential field is approximated as $\varphi_i^h(\vec{x},t) = [N(\vec{x})]\{\varphi(t)\}$, the Lagrange multiplier as $\lambda_i^h(\vec{x},t) = [N(\vec{x})]\{\lambda(t)\}$, and the test function as $w^h = [N(\vec{x})]\{w\}$. Substituting the approximations for the field variables and then canceling the factor $\{w\}$ that is common to each of the integrals, we write the semi-discretized form for the weak transport problem (2.20) as

$$\int_{\Omega_E} [N]^T[N]\{\dot{c_i}\}d\Omega + \frac{z_i F}{RT}\int_{\Omega_E} [\nabla N]^T D_i \nabla\varphi [N]\{c_i\}\, d\Omega + \int_{\Omega_E} [\nabla N]^T D_j [\nabla N]\{c_i\}\, d\Omega + z_i \int_{\Omega_E} [N]^T[N]\{\lambda\}\, d\Omega = \int_{\Omega_E} [N]^T q_i\, d\Omega - \int_{\Gamma_N} [N]^T f\, d\Gamma \tag{1.35}$$

Similarly, we multiply the electroneutrality condition (2.5) by $v \in L^2(\Omega_E)$ and integrate over the domain to get

$$\int_{\Omega_E} v \sum_{i=1}^{n} z_i c_i\, d\Omega = 0 \tag{1.36}$$

Then, substitute the approximation for the scalar fields in the above equation to obtain the discretized form for the electroneutrality constraint as

$$\int_{\Omega_E} [N]^T \sum_{j=1} z_j [N]\{c_j\}\, d\Omega = 0 \tag{1.37}$$

Equation (1.35) and Equation (1.37) form the system of equations from which approximations for the field variables c_i and λ are obtained. The semi-discrete

system of equations describing ionic transport can be expressed in matrix form as

$$\begin{bmatrix} [M] & \dots & 0 & 0 \\ \vdots & \vdots & \vdots & \vdots \\ 0 & \dots & [M] & 0 \\ 0 & \dots & 0 & 0 \end{bmatrix} \begin{Bmatrix} \{\dot{c}_1\} \\ \vdots \\ \{\dot{c}_n\} \\ 0 \end{Bmatrix} + \begin{bmatrix} [A_1] & \dots & 0 & [G_1]^T \\ \vdots & \vdots & \vdots & \vdots \\ 0 & \dots & [A_n] & [G_n]^T \\ [G_1] & \dots & [G_n] & 0 \end{bmatrix} \begin{Bmatrix} \{c_1\} \\ \vdots \\ \{c_n\} \\ \{\lambda\} \end{Bmatrix} = \begin{Bmatrix} \{F_1\} \\ \vdots \\ \{F_n\} \\ 0 \end{Bmatrix} \tag{1.38}$$

The matrices in Equation (2.23) are defined as

$$[A_i] = \frac{z_i F}{RT} \int_{\Omega_E} D_i [\nabla N]^T \nabla \varphi [N] \, d\Omega + \int_{\Omega_E} [\nabla N]^T D_i [\nabla N] \, d\Omega \tag{1.39}$$

$$[G_i] = \int_{\Omega_E} z_i [N]^T [N] \, d\Omega \tag{1.40}$$

$$[M] = \int_{\Omega_E} [N]^T [N] \, d\Omega \tag{1.41}$$

$$[F_i] = \int_{\Omega_E} [N]^T q_i \, d\Omega - \int_{\Gamma_N} [N]^T f_i \, d\Gamma \tag{1.42}$$

The system of equations in (2.23) contains the time derivative of the concentration fields. To integrate in time, we have used in this work the Crank-Nicolson method. Depending on the chemical reactions present in the domain, the system of equations in (2.23) could be nonlinear due to the production term q_i present in F_i (1.42). For these nonlinear cases, we have used a Newton-Raphson scheme.

It is important to notice that in the system of equations (2.23) the coefficient matrix consisting of blocks $[A_i]$, $[G_i]$, and $[G_i]^T$ is indefinite. However, these indefinite systems have been well studied in the finite elements literature[11], and the criteria for their stability is well understood.

Before we develop the weak formulation for the homogeneous Gauss' law (1.29), we need to specify the boundary conditions for the electric potential field. Similar to the concentration fields, the Dirichlet condition for φ is written as

$$\varphi = \varphi_0 \quad \text{on} \quad \Gamma_D \tag{1.43}$$

and over the boundaries where the concentration flux values are specified, we have the following condition [16]

$$\nabla\varphi \cdot \vec{n} = -\frac{\vec{j} \cdot \vec{n}}{\kappa} - \frac{F}{\kappa} \sum_{i=1}^{n} z_i D_i \nabla c_i \cdot \vec{n} \quad \text{on} \quad \Gamma_N \tag{1.44}$$

where κ is the conductivity given as $\kappa = F^2 \sum_{i=1}^{n} \frac{D_i}{RT} z_i^2 c_i$ and $\vec{j}$ is the current density. Multiplying Equation (1.29) with $\hat{w} \in H^1(\Omega_E)$, $\hat{w} = 0$ over Γ_D, and then using Gauss' divergence theorem, we obtain

$$\int_{\Omega_E} \nabla\hat{w} \cdot \nabla\varphi \, d\Omega_E = -\int_{\Gamma_N} \hat{w} \Big(\frac{\vec{j} \cdot \vec{n}}{\kappa} + \frac{F}{\kappa} \sum_{i=1}^{n} z_i D_i \nabla c_i \cdot \vec{n} \Big) d\Gamma \tag{1.45}$$

Substituting the finite element approximation for φ into Equation (2.28), we get

$$[K]\{\varphi\} = \{F_\varphi\} \tag{1.46}$$

where

$$[K] = \int_{\Omega_E} [\nabla N]^T [\nabla N]\{\varphi\} \, d\Omega_E \tag{1.47}$$

and

$$\{F_\varphi\} = -\int_{\Gamma_N} [N]^T \Big(\frac{\vec{j} \cdot \vec{n}}{\kappa} + \frac{F}{\kappa} \sum_{i=1}^{n} z_i D_i [\nabla N]\{c_i\} \cdot \vec{n} \Big) d\Gamma \tag{1.48}$$

We point out that the solution to concentration fields are dependent on the electric potential field φ through the coefficient matrices $[A_i]$ defined in (1.39), and the solution to φ is dependent on the concentration fields c_i through the conductivity κ in the forcing vector $\{F_\varphi\}$. Hence, Equations (2.23) and (2.29) form a fully coupled system of equations. In this work, we have used a simple Gauss-Seidel iterative method to solve the coupled system. This algorithm is given as

1. Start with an initial guess for the potential field φ.
2. Solve the system of equations (2.23) for c_i and λ.

3. Using the solution to (2.23) solve Equation (2.29) for φ.

4. Evaluate the residual for (2.23) using the solution from (2.29).

5. If residual < tolerance then finish, else go back Step 2.

1.4 Results and Discussion

The aim of this section is to verify that the finite element formulation presented in the previous section yields adequate approximations and to study the validity of the proposed mathematical model. For verification, we discuss the success of our iterative solution approach in achieving low numerical residuals. Furthermore, we study the distribution of concentration fields, electric potential fields and the interionic flux density as captured by the proposed approach. To show the validity of our mathematical model, we illustrate the importance of the interionic flux term in our proposed model by computing energy dissipation due to independent flow and interionic flow. We use the ratio of these energies to discern their relative importance in ionic transport for a given problem.

In the first example, we consider a rectangular electrolyte domain Ω_E as shown in Fig. 1.1. We used an initial concentration of 0.01 M NaCl in Ω_E and a zero flux condition over the boundary Γ_0. A constant influx of $10^{-6}\,\text{Moles}\,\text{m}^{-2}\,\text{s}^{-1}$ of Na^+ was prescribed on the boundary Γ_1, and an influx of $10^{-6}\,\text{Moles}\,\text{m}^{-2}\,\text{s}^{-1}$ of Cl^- was prescribed across the boundary Γ_2. The diffusion coefficient used for Na^+ was $1.33 \times 10^{-3}\,mm^2\,s^{-1}$, and that for Cl^{-1} was $2.03 \times 10^{-3}\,\text{mm}^2\,s^{-1}$ [26].

We studied the performance of our finite element implementation by monitoring the convergence of the numerical solutions with successive mesh and

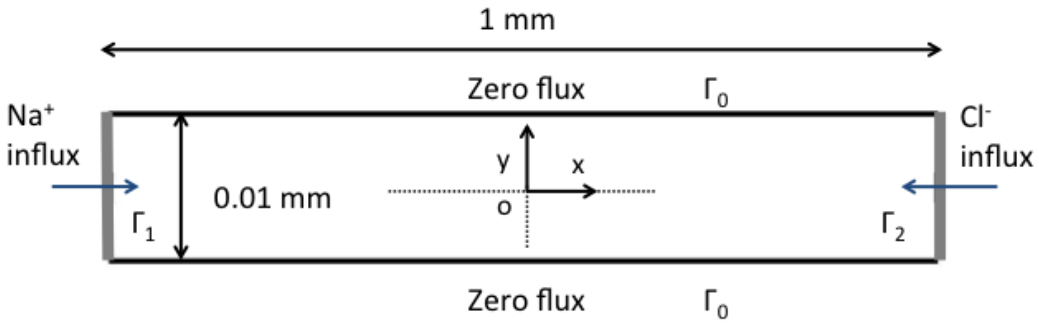

Figure 1.1: An one-dimensional electrochemical system with fixed flux values at both the boundaries

time step refinements. Our numerical results showed that the approximate solutions obtained using our numerical scheme converged in time and space as expected from the theory of finite elements. These results are not reported herein for the sake of brevity and focus. The iterative Gauss-Seidel scheme, as described in the previous section, was executed with a tolerance of 10^{-10}, which was deemed sufficient to achieve an accurate concentration distribution. We used second order quadratic elements for discretization, and we computed the transient solution for the electrochemical system with a time step of 5×10^{-4} s.

Fig. 1.2 shows the concentration distribution for the Na^+ and the Cl^- ions along the length of the domain specified in Fig. 1.1. We have shown the concentration distribution for multiple time steps with the first one being at 0.5 s and the last one at 45 s. Only one curve is shown at each time since the concentration profiles for both ions were exactly the same at every time step, as expected from the electroneutrality condition. This result verifies that the latter is indeed satisfied in our proposed formulation.

Fig. 1.3 shows the evolution of the electric potential field across the domain. We can observe that with increasing time the magnitude of the potential gra-

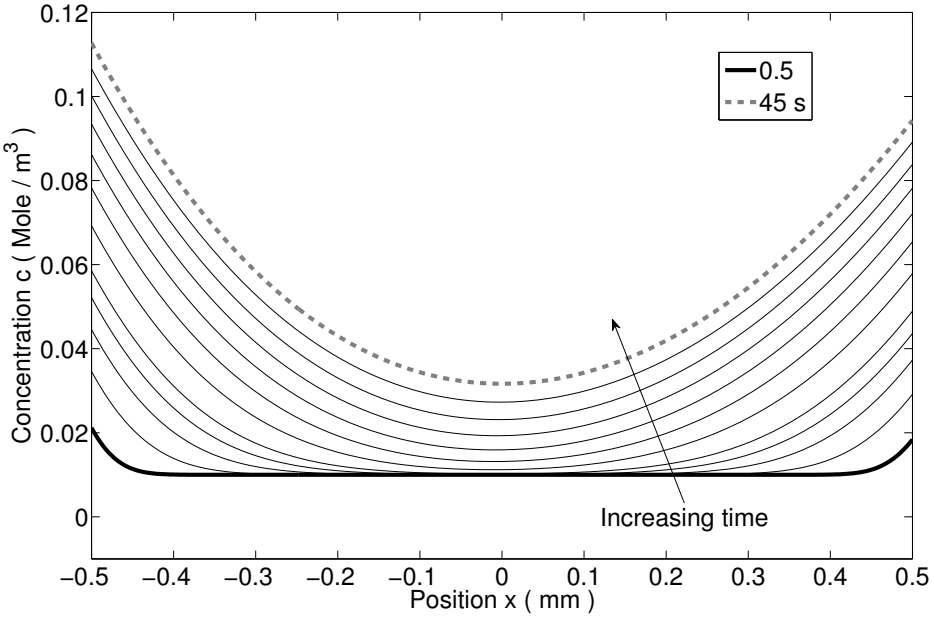

Figure 1.2: Concentration distribution along the length of the domain for multiple time steps

dient decreases. The latter trend is as expected since a constant current was specified at the boundaries, and as more ions accumulate in the domain with time, the conductivity increases and a smaller gradient is required to maintain the same current. It can also be observed that the difference in the potential distribution between successive time intervals is larger at early times, but it diminishes with time. This behavior is also expected because the magnitude of the flux relative to the existing concentration in the domain decreases with time. Hence, as the system evolves in time, the rate of change in conductivity diminishes in magnitude with respect to its existing value.

The evolution of the Lagrange multiplier field λ across the length of the domain is shown in Fig. 1.4. It is important to recall that in our formulation this field is proportional to the flux density required to maintain electroneutrality in

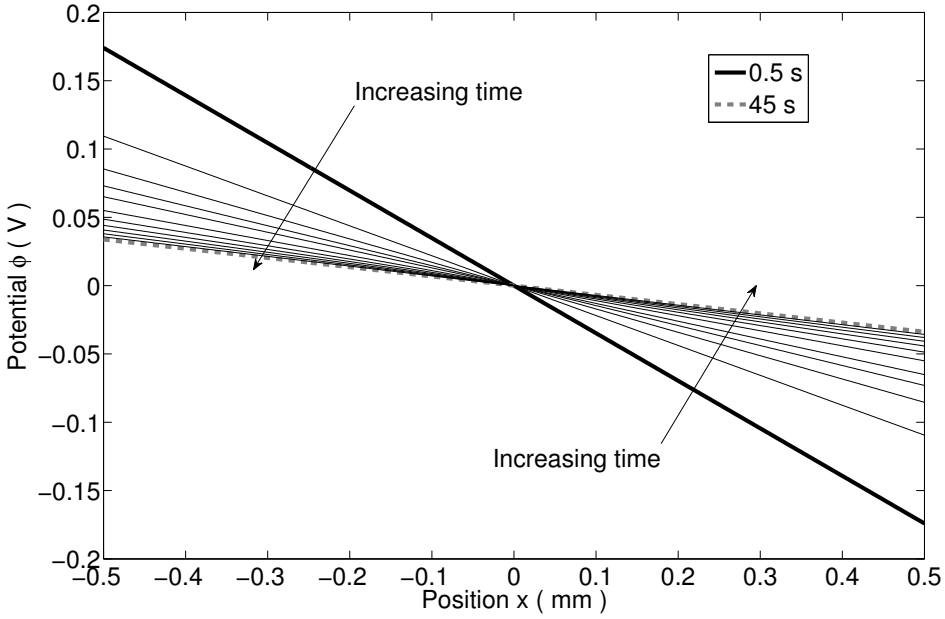

Figure 1.3: Electric potential field distribution along the length of the domain for multiple time steps

ionic transport. The plots in Fig. 1.4 show that at early times the magnitude of λ is high near the flux boundaries and drops sharply away from these boundaries. This behavior is expected as these boundaries are sources of charged species, which requires a strong counteraction by the field λ to maintain electroneutrality. Furthermore, at early times, the accumulation of charged specifies is restricted to a region near the boundaries. As time advances, the ionic fluxes propagate toward the middle of the domain and the magnitude of λ increases, as expected. Near the middle of the domain, the fluxes due to migration and diffusion are small as noticed from the small slope in the concentration fields shown in Fig. 1.2. Hence the net charge accumulation rate should be lower as compared to that at the boundaries and, consequently, the magnitude of λ should be lower. This explains the linear drop in the value of λ from both ends

at later times.

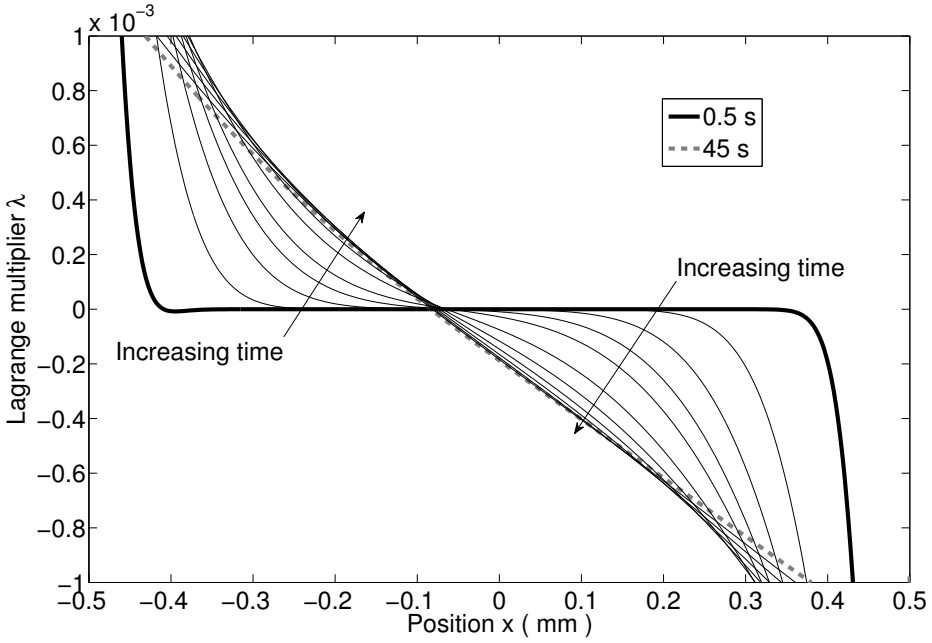

Figure 1.4: Lagrange multiplier field distribution along the length of the domain for multiple time steps

At a point in the domain where the independent flux (*i.e.* due to migration and diffusion only) of sodium ions equals the independent flux of chloride ions, electroneutrality is satisfied without the need of any additional flux term, and at this point λ should be zero. We observe such a point in Fig. 1.4 near the center of the domain. As observed from the plot at the last time step, this point is located near $x = -0.1$ mm, which is slightly shifted towards the sodium boundary. This can be explained because the mobility of the Cl^- ions is higher than that of the Na^+ ions. In the next subsection, we present a more detailed discussion on the interionic flux densities defined by λ for each of the ions.

1.4.1 Charge redistribution using interionic coupling

In Fig. 1.5, we present the distribution of the chemical potential μ_{Na^+} and the interionic flux density r_{Na^+}, and in Fig. 1.6 we present a similar plot for μ_{Cl^-} and r_{Cl^-}. Both the plots correspond to the last time step in our simulation. So, Figures 1.5 and 1.6 display the changes in the chemical potentials and the interionic flux densities across Ω_E from the sodium boundary(Γ_1) to the chloride boundary(Γ_2). The values of chemical potential for both the ions have been scaled for easy comparison with the interionic flux densities.

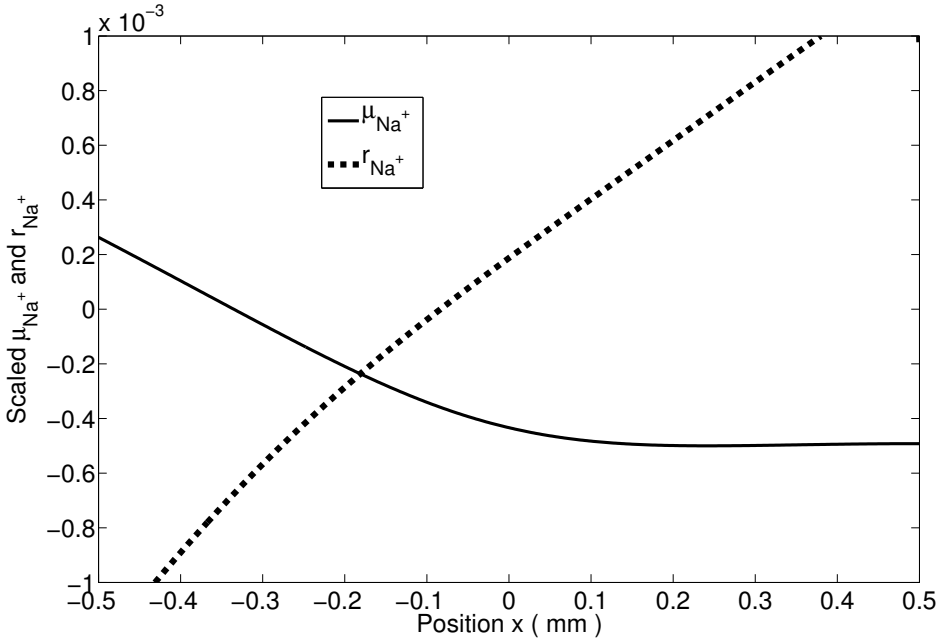

Figure 1.5: Chemical potential and interionic flux density of Na^+ along the length of the domain

Recall that the gradient of μ_{Na^+} near Γ_1 determines the independent flow (*i.e.* does not include ionic interactions) of sodium ions away from this boundary. Furthermore, the sodium boundary Γ_1 is a site for the introduction of positive ions. This introduction of positive charges repels the positive ions already

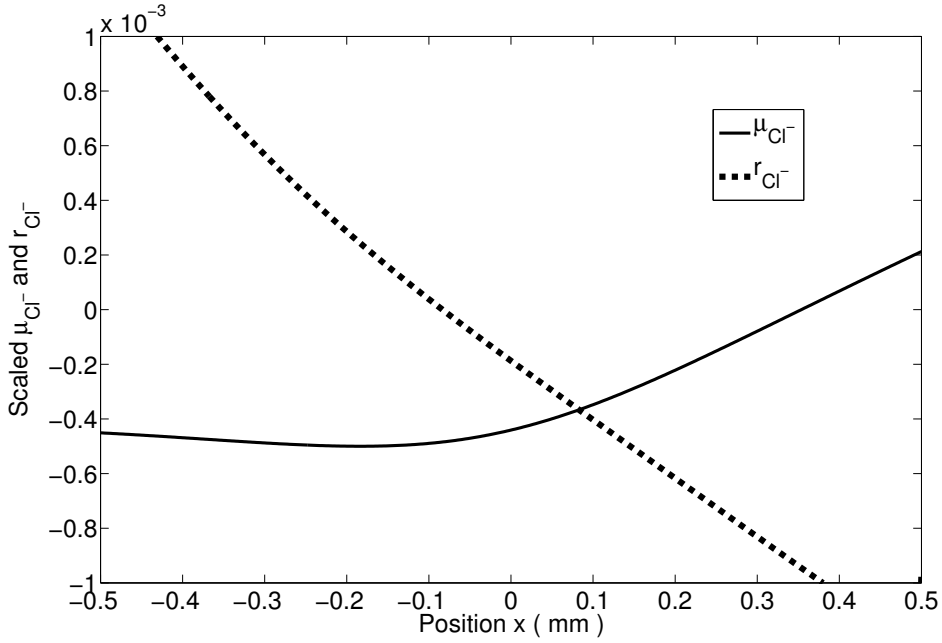

Figure 1.6: Chemical potential and interionic flux density of Cl^- along the length of the domain

present near Γ_1 and attracts the negative Cl^- ions through Coulombic interactions. These interactions produce a flux in addition to the one due to the gradient of electrochemical potential μ_{Na^+}. This flux is described by the negative values of r_{Na^+} and positive values of r_{Cl^-} near the boundary Γ_1. Since r_i is the interionic flux density, a positive r_i corresponds to inflow, and a negative r_i corresponds to outflow at a point. Repulsive forces are expected to decrease the ionic concentration at a point in the domain, and the attractive forces are expected to increase it. The latter observation explains the trends of r_{Na^+} and r_{Cl^-} obtained near the Γ_1 boundary. On the other hand, Cl^- ions are introduced at the Γ_2 boundary. Hence, the Coulombic interactions at this site repel the Cl^- ions, and attract the Na^+ ions. This behavior is reflected in the positive values of r_{Na^+} and negative values of r_{Cl^-} near Γ_c, respectively.

In order to gain further insight on how attractive and repulsive interionic forces are manifested through the flux term r_i, we use Equation (1.23) and $r_i = -z_i\lambda$ to obtain

$$\lambda = \frac{\rho_I}{\sum_{i=1}^{n} z_i^2} \tag{1.49}$$

As defined in a previous section, ρ_I is the net charge accumulation due to independent flow. From Equation (1.49), it is evident that at any point in Ω_E, λ has the same sign as ρ_I. Hence, λ is positive if there is a net accumulation of positive charge due to independent flow. The interionic flux density, r_i, is related to ρ_I as

$$r_i = -z_i \frac{\rho_I}{\sum_{i=1}^{n} z_i^2} \tag{1.50}$$

Equation (1.50) shows that if $\rho_I > 0$, then the positive ions($z_i > 0$) have a negative interionic flux density, and the negative ions($z_i < 0$) have a positive interionic flux density. The above arguments explain the way attraction and repulsion is captured in the interionic flux densities r_i. Notice that the flow of ions due to interactions tends to neutralize the resulting charge accumulation due to independent flow, which in essence, leads to electroneutrality.

1.4.2 Dissipation function

The importance of including ionic interactions can also be appreciated from the energy dissipation function. According to Onsager[17], the energy dissipation function due to ionic flow is given as

$$\Phi = \frac{1}{2} \sum_{i=1}^{n} \sum_{j=1}^{n} L_{ij} \nabla\mu_i \cdot \nabla\mu_j \tag{1.51}$$

where Φ represents the density of dissipation. Integrating Equation (1.51) over Ω_E, we obtain the total loss in Gibbs free energy (G) per unit time as

$$\Psi = \frac{1}{2}\int_{\Omega_E}\sum_{i=1}^{n}\sum_{j=1}^{n} L_{ij}\nabla\mu_i\cdot\nabla\mu_j\, d\Omega \tag{1.52}$$

where $\Psi = -\dot{G}$. The dissipation function Φ considers ionic flow in a general case. For an independent flow of ions, the cross-coefficients are assumed to vanish. So, the dissipation function for independent flow becomes

$$\Phi_I = \frac{1}{2}\sum_{i=1}^{n} L_{ii}|\nabla\mu_i|^2 \tag{1.53}$$

where the subscript I denotes independent flow, and $L_{ii} = \frac{D_i}{RT}c_i$. Correspondingly, the free energy loss rate for the domain is

$$\Psi_I = \frac{1}{2}\int_{\Omega_E}\sum_{i=1}^{n} L_{ii}|\nabla\mu_i|^2\, d\Omega \tag{1.54}$$

Hence, we can decompose Ψ as

$$\Psi = \Psi_I + \Psi_D \tag{1.55}$$

where Ψ_D is the per unit time loss in Gibbs free energy due to the ionic interactions. In terms of the cross-coefficients L_{ij}, $i \neq j$, Ψ_D is written as

$$\Psi_D = \frac{1}{2}\int_{\Omega_E}\sum_{i=1}^{n}\sum_{j=1,j\neq i}^{n} L_{ij}\nabla\mu_i\cdot\nabla\mu_j\, d\Omega \tag{1.56}$$

where the integrand is the dissipation function Φ_D due to ionic interactions. According to Equation (1.55), the ideal flow condition is equivalent to assuming $\Psi_D \approx 0$. As we have shown in Section 1.3.1, we can split the flux $\vec{J_i}$ into the ideal and the interionic components as

$$\vec{J_i} = L_{ii}\vec{\mathcal{F}_i} + \vec{Q_i} \tag{1.57}$$

where $\vec{Q}_i$ is the component of flux due to cross-coefficients. Using Equation, (1.12) $\vec{Q}_i$ is related to r_i as

$$r_i = -\nabla \cdot \vec{Q}_i \tag{1.58}$$

In our formulation, we are modeling the effect of the cross-coefficients in terms of r_i. Hence, we need to derive an expression for Ψ_D in terms of the interionic flux densities r_i. For a thermodynamic system, the change in Gibbs free energy [14] is given as

$$dG = VdP - S\,dT + \sum_{i=1}^{n} \mu_i dN_i \tag{1.59}$$

where dN_i is the change in the amount ion i in moles. At constant temperature and pressure, it simplifies to

$$dG = \sum_{i=1}^{n} \mu_i dN_i \tag{1.60}$$

Considering a differential volume, and taking the rate of change of the above expression, we obtain

$$\frac{\partial \dot{G}}{\partial V} = \sum_{i=1}^{n} \mu_i \dot{c}_i \tag{1.61}$$

Since the dissipation function represents the total rate of loss of free energy per unit volume, we have $\Phi = \frac{\partial \dot{G}}{\partial V}$. Using Equation (1.61), we can identify the dissipation due to the interionic fluxes as the contribution to $\dot{c}_i$ from r_i. Hence, the expression for dissipation Φ_D in terms of the interionic flux densities r_i is

$$\Phi_D = -\sum_{i=1}^{n} \mu_i r_i \tag{1.62}$$

Correspondingly,

$$\Psi_D = -\int_{\Omega_E} \sum_{i=1}^{n} r_i \mu_i \, d\Omega \tag{1.63}$$

So, the total dissipation in Ω_E, in terms of the independent flow, and the interionic flux densities is

$$\Psi = \frac{1}{2} \int_{\Omega_E} \sum_{i=1}^{n} L_{ii} |\nabla \mu_i|^2 \, d\Omega - \int_{\Omega_E} \sum_{i=1}^{n} r_i \mu_i \, d\Omega \tag{1.64}$$

The expression for total energy dissipation given in (1.64) shows that it simplifies to the dissipation for ideal flow (1.53) when $r_i = 0$ for all the ions. Hence, the proposition to minimize the magnitude of r_i, coupled with Equation (1.13), is equivalent to minimizing the contribution of ionic interactions to the energy dissipation function. This also justifies the use of a constrained functional (Equation (1.25)) to consider the ionic interactions that result in electroneutrality. For a fixed distribution of the chemical potentials, μ_i, minimizing the constrained functional (1.25) yields the least contribution of Ψ_D to Ψ that is required to maintain electroneutrality. Analogous to the total dissipation, we can write the dissipation function in terms of r_i as

$$\Phi = \frac{1}{2}\sum_{i=1}^{n} L_{ii}|\nabla\mu_i|^2 - \sum_{i=1}^{n} r_i\mu_i \tag{1.65}$$

Dissipation due to ionic interactions is expected to be weak in regions where ionic fluxes are low. We want to identify regions in the electrochemical domain Ω_E where the contribution to dissipation due to interactions is less than, for instance, 50% of the dissipation due to the independent flow. We accomplish this by defining a dissipation ratio γ as

$$\gamma = \begin{cases} \left|\frac{\Phi_D}{\Phi_I}\right| & \text{if } \left|\frac{\Phi_D}{\Phi_I}\right| < 0.5 \\ 0.5 & \text{if } \left|\frac{\Phi_D}{\Phi_I}\right| \geq 0.5 \end{cases} \tag{1.66}$$

Fig. 1.7 shows the ratio γ over the domain, computed along the X-axis defined in Fig. 1.1, from Γ_1 to Γ_2. We expect that at any point where the interionic fluxes are low (*i.e.* ionic interactions are weak) the ratio of Φ_D to Φ_I should be small. It can be seen from Fig. 1.7 that this ratio is low near the middle of the domain($x = 0$), which is as far as possible from either of the ionic sources. Also, notice that the value of γ drops faster from the sodium boundary towards the center than it does from the chloride boundary towards the center. This can be attributed to the lower diffusivity of sodium ions since we have specified the

same flux values for both ions. That is, the lower diffusion constant for sodium ions causes the effect of charge accumulation to spread over a smaller distance from the Boundary Γ_1 than from the Boundary Γ_2.

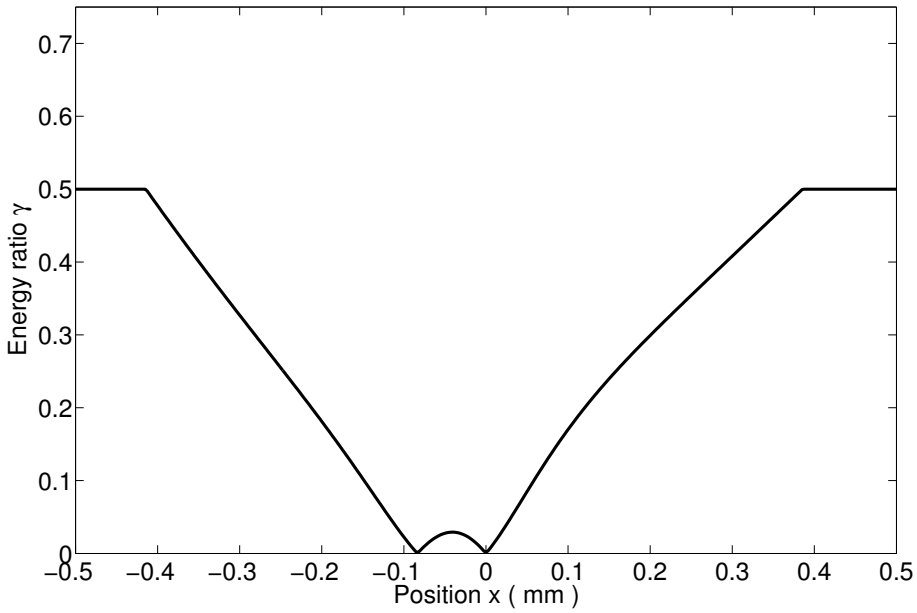

Figure 1.7: Ratio of the dissipation due to ionic interactions to the dissipation due to independent flow

The energy ratio, γ, depends on the magnitude of ionic fluxes. That is, the larger the flux value the larger the change in the electrical energy and the larger the dissipation due to Coulombic interactions. Hence, we expect that near the electrodic boundaries the contribution of Φ_D to Φ be significant. But, as we move away from the ionic sources, the flux of ions grows relatively weaker, and the ionic interactions can be assumed to be almost negligible compared to the independent flow. These trends can be observed in the plot of Fig. 1.7. Notice that the energy ratio is large near the boundaries where there is a large ion source and drops nears zero towards the center where the ionic fluxes are low. Hence,

we can conclude from these results that our proposed mathematical formulation can adequately capture both the mass transport due to ionic interactions and transport due to independent flow of ions. We end this section stating that though there exist regions in an electrochemical domain where independent flow of ions is a good approximation, it is difficult to identify these regions a priori. As shown in our results, ionic interaction becomes very relevant near boundaries that act as sources of ions.

1.4.3 Potential-time characteristic

We present a second example where we compute the electric potential-time characteristic for an electrochemical system including electrodic reactions. The purpose of this example is to verify that our proposed approach yields meaningful results when nonlinear boundary conditions are considered. We have constructed this example following the experiment reported by Dibbs, Ives, and Pittman[4] in as much as was possible. The problem in this example is the anodization of mercury at a Calomel electrode operating under a constant current in a 0.01 N HCl solution. The diagram of the 5 cm by 2 mm rectangular domain is shown in Fig. 1.8. We have divided the boundary into three parts: Γ_0, Γ_1, and Γ_2. Over the Boundary, Γ_0 we have specified a zero flux condition, which prevents any transfer of ions across this boundary. Across the Boundary Γ_2 we specify a fixed current density j, and at the boundary Γ_1 we specify a Butler-Volmer boundary condition [16] for the Calomel electrode, which is stated as

$$j = j_o(c_{Cl^-})\left\{ \exp\left[\frac{-\alpha nF}{RT}(\varphi - \varphi_o)\right] - \exp\left[\frac{(1-\alpha)nF}{RT}(\varphi - \varphi_o)\right]\right\} \tag{1.67}$$

where φ_0 is the open circuit potential, φ is the value of the electric potential field at the boundary Γ_1, n is the number of electrons transferred during the reaction,

which is 2 for this example, α is the symmetry factor, and $j_0(c_{Cl^-})$ is the open circuit current density at the concentration c_{Cl^-}. The concentration dependence of the open circuit-current density[16] is given as

$$j_0(c_{Cl^-}) = \left(\frac{c_{Cl^-}}{c^0_{Cl^-}}\right)^{2\alpha} j_0(c^0_{Cl^-}) \tag{1.68}$$

where $c^0_{Cl^-}$ is the initial concentration of chloride ions at the electrode. We used a Calomel voltage of 0.511 V as specified in [4]. The exact Tafels constant for 0.01 N HCl were not specified in [4], so we assumed a value of -0.0594 V, which corresponds to a symmetry factor of 0.5 [12]. The initial value of overpotential for this system for a net current density of 3.6×10^{-3} Am^{-2} was taken as 0.031 V as given in [4]. We have used this data to obtain an initial value of the open circuit current density as 10^{-3} Am^{-2}. The diffusion coefficient used for H^+ and Cl^- were $9.31 \times 10^{-9}\, m^2 s^{-1}$ and $2.310 \times 10^{-9}\, m^2 s^{-1}$[26], respectively. The assumed temperature was $300K$. Using these parameters, we have computed the potential-time characteristic for the system for different values of fixed current densities across Γ_2. The total simulated time was 1000 s with time steps of 0.2 s.

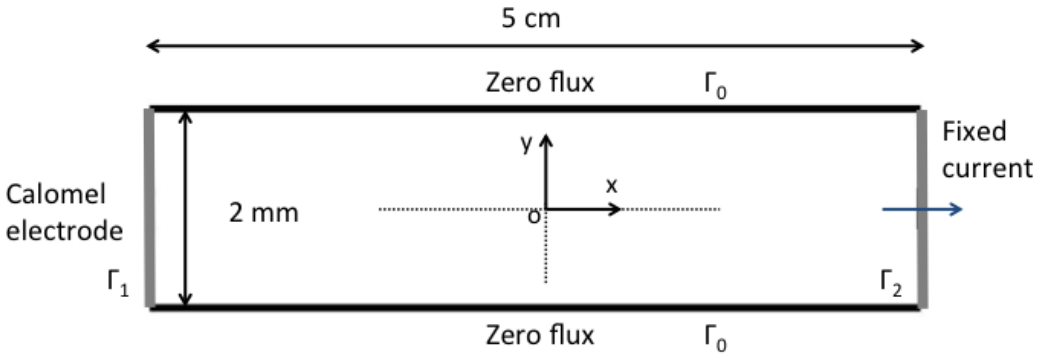

Figure 1.8: A simplified model of anodization at a Calomel electrode under a fixed current density

Fig. 1.9 shows the potential-time characteristic corresponding to 4 different

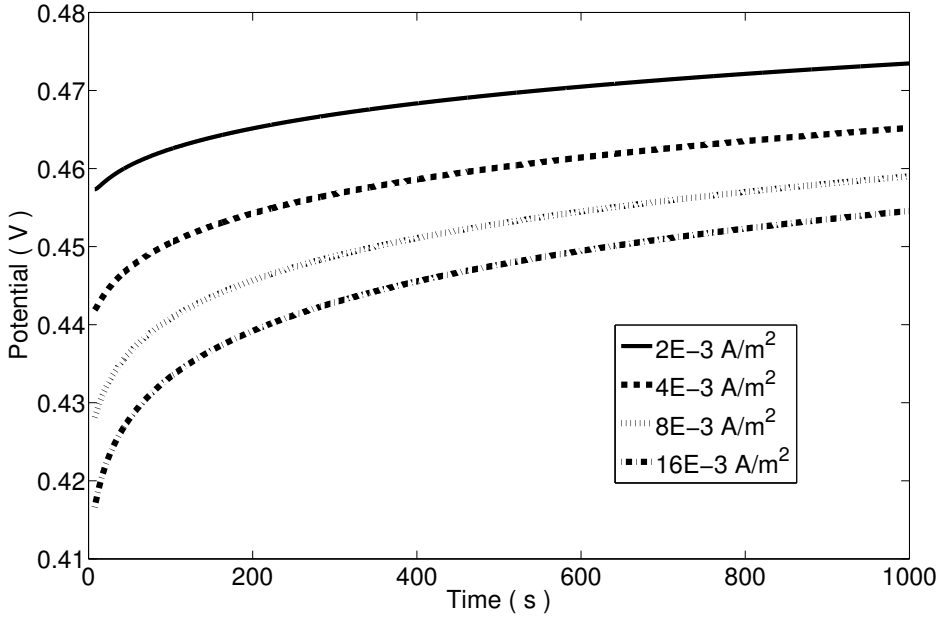

Figure 1.9: Evolution of the Calomel electrode potential with time for different values of current density

current densities. For all cases, the potential at the electrode increases monotonically with time. This behavior agrees with the experimental results reported in [4]. The observed increase in the potential can be explained as follows. As time evolves, the concentration of Cl^- ions increases near the Calomel electrode, which increases (see Equation (1.68)) the open circuit current density at the electrode. In turn, an increase in open circuit current density, implies a decrease in the overpotential in order to maintain a constant net current density. Moreover, we observe that the starting value for the potential curves decreases with increasing net current density. The reason for this drop in the initial potential is due to an increase in the magnitude of the overpotential in order to maintain a higher current density. Notice that the overpotential is a negative quantity. So, an increase in overpotential implies a decrease in the electrode potential.

1.4.4 Remarks

We have shown that our proposed mathematical model and the corresponding finite element scheme can yield results that are consistent with the expected physico-chemical behavior of the example systems analyzed in this work. However, we would like to recognize that validation of our model using experiments is of paramount importance to ascertain its accuracy in determining interionic flow in the presence of strong ionic interactions. The authors will pursue this validation in future work. Furthermore, a more general, and perhaps accurate, approach to model flow due to ionic interactions is to use measured values of the cross-coefficients in Equation (2.4). But, considering the difficulty in experimentally obtaining these values for an arbitrary mixture of ions, we have tried to make the best use of a common phenomenological observation(*i.e.* electroneutrality) to develop a mathematically consistent model. One of the shortcomings of our model is the fact that the interionic flux densities of all the ions are dependent on a single field, λ. Notice that since we have only one additional equation in the form of electroneutrality, we can just hope to obtain only one additional field from this formulation.

1.5 Conclusion

In this work, we proposed a simple mathematical model that defines the extent of interactions in ionic flow by using the electroneutrality condition as a constraint (1.25) in a variational formulation. The resultant set of equations connects the transport equation, the electroneutrality condition, and Gauss' law to solve for the concentration fields, the electric potential field, and the interi-

onic flux densities. When independent flow of ions causes an accumulation of charges, the Lagrange multiplier in our formulation determines the interionic flux densities that neutralizes this charge accumulation.The values of interionic flux densities were used to compute the free energy dissipation due to ionic interactions. The magnitude of dissipation due to interactions was compared with respect to the dissipation due to independent flow. The comparison revealed that the contribution of interactions to ionic flow is significant near the ionic sources. Whereas away from these sources, this contribution diminishes, and ionic flow could be assumed to be independent.

1.6 Acknowledgment

This work was possible due to the kind support of the National Science Foundation through Award #CAREER-0643618.

Bibliography

[1] R.G. Bartle and R.G. Bartle. *The elements of integration and Lebesgue measure*. Wiley Online Library, 1995.

[2] R.P. Buck. Kinetics of bulk and interfacial ionic motion: microscopic bases and limits for the nernstplanck equation applied to membrane systems. *Journal of Membrane Science*, 17(1):1–62, 1984.

[3] C. Dan, B. Van den Bossche, L. Bortels, G. Nelissen, and J. Deconinck. Numerical simulation of transient current responses in diluted electrochemical ionic systems. *Journal of Electroanalytical Chemistry*, 505(1):12–23, 2001.

[4] H.P. Dibbs, D.J.G. Ives, and R.W. Pittman. 670. anodic processes. part iv. the anodic generation of calomel. *J. Chem. Soc.*, pages 3370–3377, 1957.

[5] L.C. Evans. *Partial differential equations*. AMS, 1st edition, 2008.

[6] L.C. Evans. *Partial differential equations*. AMS, 1st edition, 2008.

[7] L.C. Evans. *Partial differential equations*. AMS, 1st edition, 2008.

[8] S.W. Feldberg. On the dilemma of the use of the electroneutrality constraint in electrochemical calculations. *Electrochemistry Communications*, 2(7):453–456, 2000.

[9] S. Gavrilov, M. Vankeerberghen, G. Nelissen, and J. Deconinck. Finite element calculation of crack propagation in type 304 stainless steel in diluted sulphuric acid solutions. *Corrosion Science*, 49(3):980–999, 2007.

[10] K. Hebert and R.C. Alkire. Dissolved metal species mechanism for initiation of crevice corrosion of aluminum ii. mathematical model. *Journal of the Electrochemical Society*, 130(5):1007–1014, 1983.

[11] T.J.R. Hughes. *The finite element method: linear static and dynamic finite element analysis*. Dover Publications, 2000.

[12] D.A. Jones. *Principles and prevention of corrosion*. Prentice Hall, 2nd edition, 1996.

[13] D.G. Luenberger. *Optimization by vector space methods*. Wiley-Interscience, 1969.

[14] D. A. McQuarrie. *Physical Chemistry: A Molecular Approach*. University Science Books, 1st edition, 1997.

[15] D.G. Miller. Application of irreversible thermodynamics to electrolyte solutions. i. determination of ionic transport coefficients lij for isothermal vector transport processes in binary electrolyte systems1, 2. *The Journal of Physical Chemistry*, 70(8):2639–2659, 1966.

[16] J. Newman and K.E. Thomas-Aleya. *Electrochemical Systems*. Prentice-Hall, 3rd edition, 2004.

[17] L. Onsager. Reciprocal relations in irreversible processes. i. *Physical Review*, 37(4):405, 1931.

[18] L. Onsager. Theories and problems of liquid diffusion. *Annals of the New York Academy of Sciences*, 46(5):241–265, 1945.

[19] L. Onsager and R.M. Fuoss. Irreversible processes in electrolytes. diffusion, conductance and viscous flow in arbitrary mixtures of strong electrolytes. *The Journal of Physical Chemistry*, 36(11):2689–2778, 1932.

[20] B. Pillay and J. Newman. Modeling diffusion and migration in dilute electrochemical systems using the quasi-potential transformation. *Journal of the Electrochemical Society*, 140(2):414–420, 1993.

[21] M. Planck. Ueber die potentialdifferenz zwischen zwei verdünnten lösungen binärer electrolyte. *Annalen der Physik*, 276(8):561–576, 1890.

[22] B.D. Reddy. *Introductory functional analysis: with applications to boundary value problems and finite elements*. Springer, 1997.

[23] B.D. Reddy. *Introductory functional analysis: with applications to boundary value problems and finite elements*. Springer, 1997.

[24] B.D. Reddy. *Introductory functional analysis: with applications to boundary value problems and finite elements*. Springer, 1997.

[25] J.R. Selman and J. Newman. Free-convection mass transfer with a supporting electrolyte. *Journal of The Electrochemical Society*, 118(7):1070–1078, 1971.

[26] L. Yuan-Hui and S. Gregory. Diffusion of ions in sea water and in deep-sea sediments. *Geochimica et Cosmochimica Acta*, 38(5):703–714, 1974.

CHAPTER 2

A NUMERICAL FRAMEWORK FOR THE MODELING OF CORROSIVE DISSOLUTION

We present in this work a numerical framework for simulating corrosive dissolution over long periods of time. Our proposed framework consists of three main elements: a novel dilute electrochemical model, a projective integration approach for obtaining the motion of the anodic front, and an adaptive remeshing scheme. One of the main challenges in modeling corrosive dissolution is the vast difference in the time scales involved. That is, ionic transport occurs at time scales that are many orders of magnitude smaller than the time scale at which the motion of dissolving fronts occurs. Based on the disparity of the time scales, we postulate that the evolution of the ionic distribution in the electrolyte as driven by a changing anodic front can be approximated as a sequence of steady states, effectively reducing the problem to a single time scale. With this simplification, we are able to use a simple explicit time integration scheme for determining the evolution of the dissolving anodes. We present demonstrative examples to show the capability of the proposed framework to capture complex electrochemical behavior in corroding systems when the motion of anodic fronts is considered.

2.1 Introduction

Dissolution is one of the fundamental mechanisms behind damage evolution in metals due to corrosion. There can be additional elements that contribute to

S. Sarkar, James E. Warner, and Wilkins Aquino, A Numerical Framework for the Modeling of Corrosive Dissolution, Corrosion Science 65 (2012), 502-511.

corrosion-induced damage, such as hydrogen embrittlement, but dissolution is an obvious consequence of the anodic reaction that is elementary in an alloy-electrolyte system [13, 19]. For engineering purposes (*e.g.* service life assessment and prediction for metallic structures), it is useful to estimate the susceptibility and the progress of dissolution in a given alloy-electrolyte configuration. Three very important factors on which the rate of dissolution depends are: the composition of the electrolyte, the composition of the alloy, and the geometric organization of the alloy microstructure(*e.g.* grain-grain boundary structure in intergranular corrosion). The current density distribution, or the corrosion rate over a changing anodic surface, is a function of at least these three factors. In this work, we present an approach that considers these factors to model the cumulative damage incurred in an alloy through dissolution. Hence, we need a mathematical model that can accurately capture ionic transport, current density at the electrodic surfaces, and motion of the anodic boundary due to mass loss (*i.e.* dissolution).

In order to compute the corrosion current density distribution over an anodic surface, we need to model the ionic transport processes in the electrolyte. Classically, the governing equations used to describe an electrolyte are the Nernst-Planck equation, for conservation of mass, and Gauss' law, for the electric field [10]. Attempts to solve these equations numerically have been met with challenges [20, 5]. Therefore, a popular and alternate approach is to use the electroneutrality condition [12, 14, 8, 17, 27] instead of Gauss' law align with the Nernst-Planck equation. However, in this work, we use a new ionic transport model, proposed by the authors in [24], which uses a variational approach and the electroneutrality condition to circumvent the numerical stiffness of Gauss' law and the Nernst-Planck equation. Furthermore, the ionic transport model

proposed by the authors can capture the effect of the ionic interactions on the concentration distribution in the electrolyte, and correspondingly on the anodic current density.

Once the corrosion current density is computed over the anodic surface from the dilute solution model, it can be used to define the motion of the corrosive front (*i.e.* mass loss at anode) with respect to time. The transient simulation of a corrosive process consists of two time scales: one for the ionic transport process, and another for the evolution of the anodic boundary. The evolution of the concentration fields due to ionic transport depends on the diffusion coefficient of the ions, and the change in alloy surface is driven by the rate of mass loss. The later is a significantly slower process than the former. Therefore, the process of corrosive dissolution is multiscale in time, and adequate numerical methods are needed that can handle this challenge.

Another significant challenge in modeling dissolution in corrosive processes is tracking the evolution of the moving anodic front in an efficient and robust way. Previous studies have used predefined anodic front shapes that evolve in proportion to the average current density on this surface [3]. For instance, Gavrilov [10] modeled crack growth in the presence of a corrosive environment by assuming a predefined shape of the crack front, computing the current density from the transport equations, and then moving the anodic crack front using the average current density. An alternate and simpler method was used by Wei [28] who assumed a hemispherical anodic surface with a spatially constant rate of corrosion. It is important to point out that there have been efforts in other areas related to modeling dissolution such as the work of Wojtan *et.al.* [6] where level-set were used, and Pidaparti *et.al.* [23] who used cellular automata. Both

of these works were aimed at simulating arbitrarily shaped corrosion surfaces, but with significant simplifications in the simulation of the electrochemical processes. Recently, Onishi *et. al.* [21] proposed an approach to model localized corrosion. In their approach, these authors used the finite volume method to solve the ionic transport and electrostatic problem, while the moving anodic front was tracked using a voxel method. The approach proposed by Onishi *et. al.* does not assume a fixed shape of the corrosion front and includes a very complete electrochemical model for the ionic transport and electrostatic problems. However, their approach does not include changes in the nature of the electronic boundaries (*i.e.* from cathode to anode and vice-versa) as corrosion progresses. Despite the current advances in modeling dissolution, to the best knowledge of the authors, there is still the need for a computational framework that can couple the electrochemical processes (*i.e.* ionic transport, evolution of current density, surface potentials, etc.) to the physical processes (*i.e.* mass loss, evolution of stress and strain from geometric changes, etc.) in realistic applications. This work represents a first step towards achieving such a general framework. It is important to emphasize that capturing the evolution of the anodic surface has not only important implications for understanding the importance of dissolution in damage processes, but also to understand the electrochemical changes that occur at electrodes as their geometry changes.

The rest of the paper is organized as follows. We present a background of our electrochemical model along with a Finite Element formulation. Then, we discuss our approach in tracking the motion of the anodic boundary and integrating over large time steps. Finally, using demonstrative examples, we show how the proposed framework can capture the sensitivity of the corrosion current to the geometric configuration of the alloy domain.

2.2 Background

We now briefly review the governing equations that describe a dilute electrochemical model proposed by the author in [24] for the sake of completeness. In the sequel, we will represent vector-valued fields with bold fonts. Consider the schematic diagram of a corroding system shown in Fig. 2.1. The domain of the electrolyte is Ω_E, the domain of the alloy is Ω_A, the anodic boundary is Γ_a, the cathodic boundary is Γ_c, and Γ_{el} is the electrolyte boundary that is not in contact with the alloy.

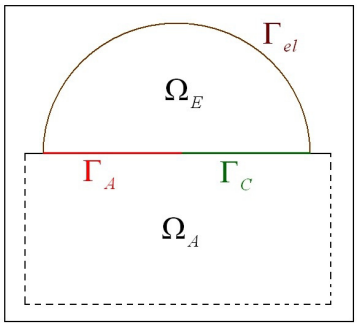

Figure 2.1: A schematic diagram of a corrosive system with the important boundaries

Let n be the number of chemical species in Ω_E. Then, the total number of field variables is $n + 1$, consisting of n concentration fields, c_i, and an electric potential field, φ. The field variables are functions of both space and time, but we have suppressed this dependence in notation for brevity. For every ion j in Ω_E, we can define a transport equation as

$$\frac{\partial c_j}{\partial t} = -\nabla \cdot \boldsymbol{J}_j + q_j \text{ in } \Omega_E, \tag{2.1}$$

where q_j is a source/sink term due to chemical reactions present in Ω_E, and $\boldsymbol{J}_j$ is the flux for ion j. The rate of production or consumption of a species due to

chemical reactions is defined through q_j as

$$q_j = \sum_{p=1}^{R} s_{jp}\left(k_{fp}\prod_{i=1}^{n} c_i^{m_{ifp}} - k_{rp}\prod_{i=1}^{n} c_i^{m_{irp}}\right) \tag{2.2}$$

where R is the number of reactions, s_{jp} is the stoichiometric coefficient for species j in reaction p, k_{fp} is the forward rate constant for reaction p, k_{rp} is the reverse rate constant, m_{fip} is the reaction order for the forward part, and m_{rip} is the reaction order for the reverse part. If a species i is absent in reaction number p, then s_{jp}, m_{ifp}, and m_{irp} are zero.

The flux $\boldsymbol{J}_j$ is given as

$$\boldsymbol{J}_j = -D_j\nabla c_j - \frac{z_j F}{RT}(D_j c_j \nabla\varphi) - \sum_{k=1,k\neq j}^{n} L_{jk}\nabla\mu_k \tag{2.3}$$

where z_j is the charge of ion j, D_j is the diffusivity (assumed to be spatially invariant in this work), F is the Faraday's constant, and μ_k is the chemical potential for ion k [20]. The quantities L_{jk}, $j \neq k$ are the Onsager's reciprocal coefficients [22], which influence the flux of ionic species j due to the thermodynamic forces $-\nabla\mu_k$, stemming from the rest of the ions. Substituting Eq. (2.3) into the transport equation (2.1), we obtain

$$\frac{\partial c_j}{\partial t} = \nabla\cdot(D_j\nabla c_j) + \frac{z_j F}{RT}\nabla\cdot(D_j c_j\nabla\varphi) + \nabla\cdot\left(\sum_{k=1,k\neq i}^{n} L_{jk}\nabla\mu_k\right) + q_j \tag{2.4}$$

Eq. (2.4) is an extension of the classical non-convective Nernst-Planck equation. Notice that the difference is the additional term $\nabla\cdot(\sum_{k=1,k\neq j}^{n} L_{jk}\nabla\mu_k)$, which arises from the Coulombic interaction among the ions.

Our approach is to use the electroneutrality condition, stated as

$$\sum_{j=1}^{n} z_j c_j = 0, \tag{2.5}$$

to enforce an additional constraint on the classical Nernst-Planck equation. Application of the constraint in (2.5) makes the ionic distributions linearly dependent, thereby incorporating the effect of the cross-coefficients(L_{jk}, $j \neq k$). For this purpose, we define an additional unknown r_j as

$$r_j = \nabla \cdot \left(\sum_{k=1, k\neq j}^{n} L_{jk} \nabla \mu_k \right), \tag{2.6}$$

which is the flux density for ion j due to the ionic interactions, and we substitute this definition into Eq. (2.4) to get

$$\frac{\partial c_j}{\partial t} = \nabla \cdot (D_j \nabla c_j) + \frac{z_j F}{RT} \nabla \cdot (D_j c_j \nabla \varphi) + q_j + r_j. \tag{2.7}$$

Notice that we now have an additional variable r_j. This new unknown is present because the ionic distributions depend on each other due to the Coulombic interactions. Motivated by the fact that the quantities r_j become zero (or have the least possible magnitude) when the ionic distributions are independent of each other, we compute the smallest magnitude of r_j that is needed for a distribution of ions constrained to satisfy the electroneutrality condition. This goal was achieved in [24] by formulating a constrained minimization problem in terms of r_j. The expression for r_j obtained from this approach is

$$r_j = -z_j \lambda, \tag{2.8}$$

where λ is a scalar field over the domain Ω_E and represents the Lagrange multiplier used to enforce electroneutrality as a constraint. Hence, the modified form for the ionic transport equation constrained to satisfy electroneutrality is given as

$$\frac{\partial c_j}{\partial t} = \nabla \cdot (D_j \nabla c_j) + \frac{z_j F}{RT} \nabla \cdot (D_j c_j \nabla \varphi) + q_j - z_j \lambda. \tag{2.9}$$

The boundary of the electrochemical domain Γ_E can be divided into four types: Dirichlet boundary Γ_D, Neumann boundary Γ_N, anodic boundary Γ_a, and

cathodic boundary Γ_c. The concentration value for a species j is specified over the Dirichlet boundaries Γ_D as

$$c_j = u_j \quad \text{on} \quad \Gamma_D. \tag{2.10}$$

Neumann boundary conditions for chemical species are defined as

$$-\frac{z_j D_j F}{RT} c_j \nabla\varphi \cdot \boldsymbol{n} - D_j \nabla c_j \cdot \boldsymbol{n} = g_j \quad \text{on} \quad \Gamma_N, \tag{2.11}$$

where $\boldsymbol{n}$ is the unit outward normal vector, and g_j is the ionic flux specified at the boundary. For an impermeable boundary, we take $g_j = 0$. Similarly, the flux of ions at the electrodic boundaries is specified as

$$-\frac{z_j D_j F}{RT} c_j \nabla\varphi \cdot \boldsymbol{n} - D_j \nabla c_j \cdot \boldsymbol{n} = f_j \quad \text{on} \quad \Gamma_a \cup \Gamma_c, \tag{2.12}$$

where f_j is proportional to the current density as given by

$$i_{a/c} = F z_j f_j, \tag{2.13}$$

and $i_{a/c}$ represents current density at the anode or cathode, depending on the boundary region. The current density is, in turn, obtained from the Butler-Volmer relations given as

$$i_a = i_{oa}\left[\exp\left(\frac{(1-\alpha_a) n_a F \eta_a}{RT}\right) - \exp\left(\frac{-\alpha_a n_a F \eta_a}{RT}\right)\right] \text{ on } \Gamma_a \tag{2.14}$$

and

$$i_c = i_{oc}\left[\exp\left(\frac{(1-\alpha_c) n_c F \eta_c}{RT}\right) - \exp\left(\frac{-\alpha_c n_c F \eta_c}{RT}\right)\right] \text{ on } \Gamma_c. \tag{2.15}$$

In the above equations, η_a and η_c are the overpotentials, α_a and α_c are the symmetry factors, i_{oa} and i_{oc} are the open-circuit current densities for a given electrode, and n_a and n_c are the number of electrons transferred during the anodic and the cathodic reactions, respectively.

The electric potential field φ appearing in the equations above satisfies Gauss' law, which is stated as

$$\nabla^2\varphi = -\frac{F}{\varepsilon}\sum_{j=1}^{n} z_j c_j, \tag{2.16}$$

where ε is the permittivity of the medium. Notice that the right hand side Eq. (2.16) becomes zero due to the electroneutrality condition (2.5). Hence, the governing equation for the electric potential field that is consistent with the electroneutrality condition is the homogenous form of Gauss' law, which is given as

$$\nabla^2\varphi = 0. \tag{2.17}$$

The electrodic boundary conditions for the electric potential field φ are given as [20]

$$\nabla\varphi \cdot \boldsymbol{n} = -\frac{i_{a/c}}{\kappa} - \frac{F}{\kappa}\sum_{p=1}^{n} z_p D_p \nabla c_p \cdot \boldsymbol{n} \quad \text{on} \quad \Gamma_a \text{ and } \Gamma_c, \tag{2.18}$$

where κ is the conductivity. This conductivity is obtained from the ionic concentration fields as

$$\kappa = F^2 \sum_{p=1}^{n} \frac{D_p}{RT} z_p^2 c_p. \tag{2.19}$$

It is important to notice that the current density, $i_{a/c}$, is obtained from Eqs. (2.14) and (2.15).

As mentioned above, we have used the condition of electroneutrality (2.5) to reduce Gauss' law from Poisson's (2.16) to Laplace's equation (2.17). Electroneutrality is an acceptable phenomenological condition for the bulk of the electrochemical domain. However, near the electrodic boundaries, electroneutrality may be violated due to the formation of the Electrical Double Layer (EDL). The region of non-zero charge density due to the EDL is approximately 10 nm in width [20]. Therefore, our proposed model is only valid for domains significantly larger than the length scale of the EDL.

2.3 Formulation

2.3.1 Finite element model

We now present a finite element model corresponding to the governing equations and the boundary conditions described in the previous section. A detailed derivation of this finite element model without the Butler-Volmer type boundary conditions can be found in [24]. The weak formulation of the transport problem is obtained by multiplying Eq. (2.9) by a test function w and applying Gauss' divergence theorem. That is, the weak form is given as

$$\begin{aligned}\int_{\Omega_E} w\dot{c_j}\mathrm{d}\Omega = &\int_{\Gamma_N\cup\Gamma_a\cup\Gamma_c} wD_j\nabla c_j\cdot\boldsymbol{n}\,\mathrm{d}\Gamma + \frac{z_jF}{RT}\int_{\Gamma_N\cup\Gamma_a\cup\Gamma_c} wD_jc_j\nabla\varphi\cdot\boldsymbol{n}\,\mathrm{d}\Gamma\\ &-\frac{z_jF}{RT}\int_{\Omega_E}\nabla w\cdot(D_jc_j\nabla\varphi)\,\mathrm{d}\Omega - \int_{\Omega_E}\nabla w\cdot(D_j\nabla c_j)\,\mathrm{d}\Omega\\ &+\int_{\Omega_E} wq_j\,\mathrm{d}\Omega - \int_{\Omega_E} wz_j\lambda\,\mathrm{d}\Omega\ \ \forall w\in\mathcal{W}\end{aligned} \tag{2.20}$$

Then, we substitute the boundary conditions in equations (2.11) and (2.12) to obtain

$$\begin{aligned}\int_{\Omega_E} w\dot{c_j}\mathrm{d}\Omega = &-\int_{\Gamma_N} wg_j\,\mathrm{d}\Gamma - \frac{z_jF}{RT}\int_{\Omega_E}\nabla w\cdot(D_jc_j\nabla\varphi)\,\mathrm{d}\Omega - \int_{\Omega_E}\nabla w\cdot(D_j\nabla c_j)\,\mathrm{d}\Omega\\ &-\int_{\Gamma_a\cup\Gamma_c} w\Big(\frac{i_{a/c}}{z_jF}\Big)\mathrm{d}\Gamma + \int_{\Omega_E} wq_j\,\mathrm{d}\Omega - \int_{\Omega_E} wz_j\lambda\,\mathrm{d}\Omega\ \ \forall w\in\mathcal{W}\end{aligned} \tag{2.21}$$

Similarly, the weak statement for the electroneutrality condition is given as

$$\int_{\Omega_E} v\sum_{j=1}^{n} z_jc_j\,\mathrm{d}\Omega = 0\ \ \forall v\in\mathcal{V} \tag{2.22}$$

where v is a test function. In the above expressions, the concentration fields belong to a function space $\mathcal{U}$. The spaces $\mathcal{U}$, $\mathcal{W}$ and $\mathcal{V}$ are suitable function spaces with enough regularity to admit the operations involved. The approximation

for the concentration field c_i is given as $c_j^h(\boldsymbol{x},t) = [N(\boldsymbol{x})]\{c_j(t)\}$ [2]. Where $[N(\boldsymbol{x})]$ is a matrix containing finite element shape functions, and $\{c_j(t)\}$ is a vector of nodal values for the concentrations of ionic species j. We define similar approximations for λ, w, and v. After substituting these approximations in Equations (2.21) and (2.22), and canceling the factors $\{w\}$ and $\{v\}$, we obtain a nonlinear system of ordinary differential equations describing ionic transport as

$$\begin{bmatrix} [M] & \dots & 0 & 0 \\ \vdots & \vdots & \vdots & \vdots \\ 0 & \dots & [M] & 0 \\ 0 & \dots & 0 & 0 \end{bmatrix} \begin{Bmatrix} \{\dot{c}_1\} \\ \vdots \\ \{\dot{c}_n\} \\ \{0\} \end{Bmatrix} + \begin{bmatrix} [A_1] & \dots & 0 & [G_1]^T \\ \vdots & \vdots & \vdots & \vdots \\ 0 & \dots & [A_n] & [G_n]^T \\ [G_1] & \dots & [G_n] & [0] \end{bmatrix} \begin{Bmatrix} \{c_1\} \\ \vdots \\ \{c_n\} \\ \{\lambda\} \end{Bmatrix} = \begin{Bmatrix} \{F_1\} \\ \vdots \\ \{F_n\} \\ \{0\} \end{Bmatrix} \tag{2.23}$$

The matrices in Equation (2.23) are defined as

$$[A_j] = \frac{z_j F}{RT} \int_{\Omega_E} D_j [\nabla N]^T \nabla\varphi [N] \, \mathrm{d}\Omega + \int_{\Omega_E} [\nabla N]^T D_j [\nabla N] \, \mathrm{d}\Omega \tag{2.24}$$

$$[G_j] = \int_{\Omega_E} z_j [N]^T [N] \, \mathrm{d}\Omega \tag{2.25}$$

$$[M] = \int_{\Omega_E} [N]^T [N] \, \mathrm{d}\Omega \tag{2.26}$$

$$\{F_j\} = \int_{\Omega_E} [N]^T q_j \, \mathrm{d}\Omega - \int_{\Gamma_N} [N]^T g_j \, \mathrm{d}\Gamma - \int_{\Gamma_a \cup \Gamma_c} [N]^T \left(\frac{i_{a/c}}{z_j F} \right) \mathrm{d}\Gamma \tag{2.27}$$

Notice that depending on the reaction orders, the source/sink term q_j for ion j can be nonlinear, and so will be the vector $\{F_j\}$ in Eq. (2.27).

The weak formulation for the homogeneous version of Gauss' law, Eq. (2.17), is obtained in a similar manner as was shown above for the transport equations. The weak statement for this problem is given as find $\varphi \in \mathcal{S}$ such that

$$\int_{\Omega_E} \nabla\hat{w} \cdot \nabla\varphi \, \mathrm{d}\Omega_E = -\int_{\Gamma_a \cup \Gamma_c} \hat{w} \left(\frac{i_{a/c}}{\kappa} + \frac{F}{\kappa} \sum_{p=1}^{n} z_p D_p \nabla c_p \cdot \boldsymbol{n} \right) \mathrm{d}\Gamma \quad \forall \hat{w} \in \overline{\mathcal{W}} \tag{2.28}$$

where $\mathcal{S}$ and $\overline{\mathcal{W}}$ are suitably defined function spaces. Notice that in the derivation of the weak formulation we have used the boundary condition given in Eq. (2.18).

Substituting a finite element approximation for φ (similar to c_j) into Equation (2.28), we obtain

$$[K]\{\varphi\} = \{F_\varphi\}, \tag{2.29}$$

where

$$[K] = \int_{\Omega_E} [\nabla N]^T [\nabla N]\{\varphi\}\, \mathrm{d}\Omega_E \tag{2.30}$$

and

$$\{F_\varphi\} = -\int_{\Gamma_a \cup \Gamma_c} [N]^T \left(\frac{i_{a/c}}{\kappa} + \frac{F}{\kappa} \sum_{p=1}^{n} z_p D_p [\nabla N]\{c_p\} \cdot \boldsymbol{n} \right) \mathrm{d}\Gamma \tag{2.31}$$

Equations (2.23) and (2.29) define the complete set of semi-discretized equations that we use to obtain the field solutions to a dilute electrochemical problem. Equation (2.23) depends on φ through the matrices $[A_j]$ and vectors $\{F_j\}$, while Equation (2.29) depends on c_j through κ. Therefore, Equations (2.23) and (2.29) form a coupled system of nonlinear ordinary differential and algebraic equations. We used an iterative Gauss-Seidel approach to find the solution to this coupled system of equations, as described in [24]. For each Gauss-Seidel iteration, we solved two nonlinear system of equations using the Newton-Raphson method [26]. The details of these approaches are outside the scope of this work and are not discussed further.

2.3.2 Dissolution of anode

Once the current density is computed, it can be used to determine the rate of mass loss over the boundary. In this section, we develop the equations that relate the current density to the motion of the anodic boundary. We start with an initial geometry at $t = 0$. Due to corrosion, the shape and the position of the anodic boundary Γ_a will evolve over time. Since this change involves the motion of a surface, it can be treated numerically as a displacement field over Γ_a driven by the corrosion rate. We define $\boldsymbol{u}(\boldsymbol{x}, t)$ as the corrosion front displacement field over Γ_a, and its time derivative $\boldsymbol{v}(\boldsymbol{x}, t) = \dot{\boldsymbol{u}}(\boldsymbol{x}, t)$ as the front velocity.

Let w_M be the atomic weight of the anodic metal. Then, the rate of anodic dissolution(*i.e.* mass loss per unit area per unit time) can be obtained from the anodic current density using Faraday's law of electrolysis [13] as

$$q_m = \frac{w_M i_a}{z_a F} \quad \text{on} \quad \Gamma_a \tag{2.32}$$

In Fig. (2.2), we show a subregion of the anodic material inside the alloy domain, including part of the anodic boundary.

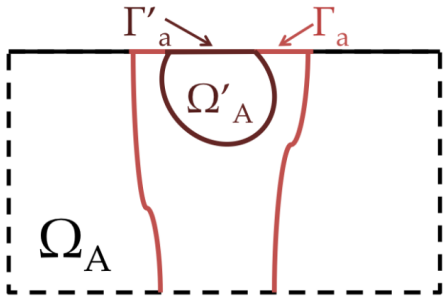

Figure 2.2: Alloy domain highlighting a subregion in the anode

We define this subregion as Ω'_A and the corresponding segment of the anodic boundary as Γ'_a. Using Reynold's Transport Theorem [2], we can express the

conservation of mass over the sub-domain Ω'_A as

$$\int_{\Omega'_A} \left(\frac{\mathrm{D}\rho}{\mathrm{D}t} + \rho \nabla \cdot \boldsymbol{v} \right) \mathrm{d}\Omega = - \int_{\Gamma'_a} q_m \mathrm{d}\Gamma \tag{2.33}$$

where $\frac{\mathrm{D}\rho}{\mathrm{D}t}$ is the material time derivative of the density. We will take the density of the alloy to be constant in time, which yields $\frac{\mathrm{D}\rho}{\mathrm{D}t} = 0$. We also assume that the density of the anodic material is spatially constant, which leads to

$$\rho \nabla \cdot \boldsymbol{v} = \nabla \cdot (\rho \boldsymbol{v}) \tag{2.34}$$

Using these assumptions and Gauss' Divergence Theorem [9], we can rewrite Equation (2.33) as

$$\int_{\Gamma'_a} (\rho \boldsymbol{v} \cdot \boldsymbol{n} + q_m) \, \mathrm{d}\Gamma = 0 \tag{2.35}$$

Since the above integral statement is true for arbitrary Γ'_a, we use the principle of localization [2] to obtain the velocity of a point on the anodic front as

$$\boldsymbol{v} \cdot \boldsymbol{n} = -\frac{q_m}{\rho} \text{ on } \Gamma_a \tag{2.36}$$

We can see from Eq. (2.36) that dissolution induces a motion that is normal to the anodic boundary. Using this equation, the corrosion velocity vector can be described in terms of the corrosion current as

$$\dot{\boldsymbol{u}}(\boldsymbol{x}, t) = -\frac{w_M}{z_a \rho F} i_a(\boldsymbol{u}, \boldsymbol{x}, t) \boldsymbol{n}(\boldsymbol{x}, t) \quad \text{on} \quad \Gamma_a \tag{2.37}$$

where we have used $\boldsymbol{v} = \dot{\boldsymbol{u}}$. Notice that Equation (2.37) is a vector-valued ordinary differential equation whose solution, $\boldsymbol{u}$, represents the geometric evolution of the anodic boundary. Since the current density distribution is itself a (nonlinear) function of the geometry of the boundary (*i.e.* i_a depends on $\boldsymbol{u}$), we can see that Eqs. (2.37) and Eq. (2.23) are fully coupled. In order to define the geometric

configuration of the anodic boundary at time t, we need to integrate Eq. (2.37). One difficulty in accomplishing this integration is that the the dependence of i_a on $\boldsymbol{u}$ is not known explicitly, in general. That is, they are related through complex nonlinear differential equations.

2.3.3 Time integration and front tracking

In this section, we describe an approach to integrate Equation (2.37) and to define the motion of the alloy-electrolyte interface. Corrosive dissolution is a slow process. The amount of time required for a significant modification in the geometry of the alloy can be in the order of days, months, or years, while changes in the concentration fields near the electrodic surfaces can occur within the span of seconds, milliseconds, or shorter times.

We can appreciate the separation of time scales involved in the problem at hand through the following simple example. Consider an Al^{3+} ion whose diffusivity is of the order of $10^{-4}\,\mathrm{mm^2 s^{-1}}$. Furthermore, assume that the length of the corroding region is of the order of $0.1\,\mu\mathrm{m}$ (grain boundary width for a typical alloy [7]). Then, the time required by the ion to traverse this distance would be in the order of $10^{-5}\,\mathrm{s}$ [4]. If a corrosion current density of $1\,\mu\mathrm{A\,cm^{-2}}$ is considered, the penetration rate would be in the order of $10^{-7}\mu\mathrm{m\,s^{-1}}$ [13]. So, the time t for which the corroding front would move $0.1\,\mu\mathrm{m}$ is of the order of $10^6\,\mathrm{s}$. The latter example demonstrates that simulating corrosive dissolution involves a vast separation of time scales. It is important to recognize that we have ignored convective transport in the above argument. However, in many practical problems convection of ionic species would also occur at much higher speeds

than the motion of the boundary due to dissolution.

Now, for computational purposes, if we used the time scale for the transport process to march through the entire time period of dissolution, then the number of time steps required would be in the order of 10^{11} for the above example. Such a large difference in the time scales may render the modeling of dissolution computationally intractable. In order to circumvent this difficulty and due to the fact that the front evolves at a much slower rate than the transport of the ionic species, we have assumed that for a given geometry, we can approximate the ionic transport problem as a steady-state process. That is, at each time in the evolution of the anodic front, we consider a steady-state ionic transport process. In other words, the rate of change of the concentrations of the ionic species becomes negligible at the time scale in which the anodic front evolves.

Using the above steady-state assumption, the time derivatives in Eq. (2.23) vanish and only the solution to a nonlinear algebraic system is needed. So, the problem reduces to a single time scale (*i.e.* the one dictated by the corrosion front velocity). However, notice that we still do not have an explicit representation of the right-hand side of Eq. (2.37). To integrate this equation, we resort to a simple projective integration scheme similar to that proposed by Gear *et al.* [11, 15].

The projective integration approach used in this paper can be described as follows. Assume that we know the position of the anodic front at time t, $\Gamma_a(t)$, and we wish to compute its position at time $t+\Delta t$, $\Gamma_a(t+\Delta t)$. We first compute the current density i_a over $\Gamma_a(t)$ by solving the steady-state transport equations and Gauss' law, and then use a Forward Euler scheme to obtain the displacement of the front as

$$\boldsymbol{u}(\boldsymbol{x}, t+\Delta t) = -\frac{w_M}{z_a \rho F} i_a(\boldsymbol{x}, \boldsymbol{u}, t)\boldsymbol{n}(\boldsymbol{x}, t)\Delta t \tag{2.38}$$

where the time step Δt is as required by the time scale for the process of dissolution, and stability of the Forward Euler scheme. Then, the updated coordinates of the spatial points defining $\Gamma_a(t + \Delta t)$ are computed as

$$\boldsymbol{x}(t + \Delta t) = \boldsymbol{x}(t) + \boldsymbol{u}(\boldsymbol{x}, t + \Delta t), \quad \forall \boldsymbol{x}(t) \in \Gamma_a(t) \tag{2.39}$$

After every time step, the electrochemical domain has to be redefined since the anodic boundary moves due to dissolution. In our current approach, we accomplish this step by displacing only the anodic nodes in the electrochemical domain as dictated by Eq. (2.38). It is important to bear in mind that displacement of these nodes may significantly distort the elements near the anodic boundary, degrading the accuracy of the numerical solution. To avoid significant element distortions, we resort to remeshing the domain at each time step. For this, we update the coordinates that define the boundary of the electrochemical domain at $t + \Delta t$ as shown in Eq. (2.39). Then, we use this information with a robust finite element mesh generator to obtain a suitable discretization of the electrochemical domain at the current time. We would like to point out that there is no need to transfer information such as potential, concentrations, etc. from the electrochemical domain at time t to the newly re-meshed domain at time $t + \Delta t$. The reason for not needing to transfer information is the vast disparity between the ionic transport time scale and the moving anode time scale. In other words, the fact that we can assume a steady-state condition of the ionic transport process at the time scale of the moving boundary eliminates the need to transfer information across domains.

It is imperative to mention a few details about the representation of the anodic surface and its impact on the stability of the proposed methodology. First, we recognize that in regions of high current density, the front velocity and the

corresponding displacement will be proportionally high. This can cause severe distortions in the finite element mesh and subsequent instabilities in the evolution of the front. That is, as distortions in the mesh occur, higher fictitious currents (gradients) are produced, and in turn larger distortions appear. This is a circular phenomenon that can lead to instabilities early in the simulation. To alleviate this problem, anodes were represented with cubic B-splines. The radius of curvature of a B-spline during the evolution of the front was used along with a heuristic rule for selecting the finite element node densities for remeshing at each time step. This was a crucial step for evolving the dissolving surfaces in a stable manner in all the examples investigated. The details of this part of our algorithm are not provided for the sake of brevity and focus.

Another important issue to consider in the evolution of the anodic front is that new cathodic or inert portions of the boundary can emerge. That is, dissolution exposes new surfaces in which the geometric organization of the anode and the cathode can be different from the one of the previous time step. In our algorithm implementation, as the anodic front evolves, its motion is constrained so that it does not penetrate into cathodic or inert regions. Furthermore, as cathodic material is exposed at each time step, the boundary conditions are changed from anodic to cathodic or inert, depending on the material exposed. This capability makes our proposed methodology suitable for simulating intergranular corrosion in complex polycrystalline configurations. It is important to realize that changes in the boundary partition introduce additional nonlinearity into the problem at hand.

A simplified description of our algorithm for evolving the anodic surface is given next.

1. Define configuration for the corrosion front at time $t = 0$.
2. Do for each time step until final time
   (a) Obtain the concentration fields c_j and the electrostatic potential φ from Eqs. (2.23) and (2.29).
   (b) Obtain the anodic dissolution rate using Eq. (2.32).
   (c) Obtain a new position for the surface Γ_a both in Ω_E and Ω_A using (2.38).
   (d) Redefine the electrodic properties according to the new position of the anodic surface.
   (e) Update the finite flement mesh for the modified electrolyte and alloy domains.

2.4 Results and Discussion

We present two numerical examples that demonstrate the feasiblity and performance of the proposed method. Both examples are based on a sensitized Al 5083 system where the grain boundary consists of the Mg-rich β phase Al_3Mg_2, which acts as the anode [7, 16, 1]. Using these two examples, we study the convergence in mass loss due to dissolution and in the anode-cathode ratio with refinement in time steps. We also demonstrate how the proposed framework can capture the sensitivity of the corrosion current density to changes in the grain-grain boundary geometry inside the alloy domain.

In both examples, we have assumed the dissolution of Mg at the Mg-rich β phase

	φ_{oa}	φ_{oc}	β_a	β_c	i_{oa}	i_{oc}
Γ_a	-1.25 V	-	0.137 V/dec	-0.0142 V/dec	10^{-5}A/m^2	-
Γ_c	-	-0.7 V	0.0291 V/dec	-0.234 V/dec	-	10^{-5}A/m^2

Table 2.1: Electrochemical properties of the electrodic boundaries [7, 18].

ion	Diffusivity (m^{2}s^{-1})	Initial Concentration (M)
Mg^{2+}	4×10^{-10}	3×10^{-7}
OH^-	4×10^{-9}	6×10^{-7}
$Mg(OH)_2$	1×10^{-9}	0.0

Table 2.2: Diffusivity and initial concentration of ions [29, 25].

$$Mg \longrightarrow Mg^{2+} + 2\,e^- \quad \text{over} \quad \Gamma_a$$

and production of OH^- at the cathodic sites

$$O_2 + 2\,H_2O + 4\,e^- \longrightarrow 4\,OH^- \quad \text{over} \quad \Gamma_c$$

The open circuit potentials, Tafel constants, and the open circuit current density values for the electrodes are listed in Table 2.1. Diffusion coefficients and the assumed initial concentration for the ions are given in Table 2.2.

We have assumed hydrolyses of Magnesium ions to be the only chemical reaction in the bulk with a solubility product of 1.5×10^{-11}, and dissolved oxygen is available in abundance throughout the electrochemical domain.

2.4.1 Example 1: Straight grain boundary

We show in Fig. (2.3) a sketch of the alloy-electrolyte system for the first example and the corresponding finite element mesh. This example simulates progressive dissolution in a straight anodic grain boundary between two cathodic grains. The anodic (Γ_a) and the cathodic (Γ_c) boundaries had an initial length ratio of 0.05. Over the remaining electrolyte boundary, Γ_{el}, we have specified Dirichlet boundary conditions (see Eq. (2.10)) for all the chemical species.

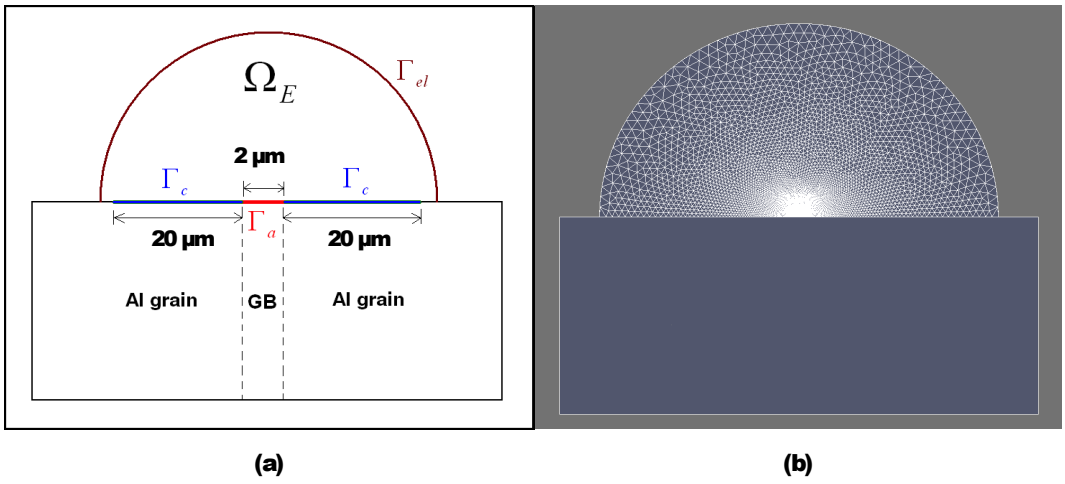

Figure 2.3: (a) Domain for Example 1. (b) Corresponding finite element mesh.

First, we studied the convergence in total mass loss due to dissolution with decreasing time steps. We computed the mass loss due to dissolution of the grain boundary for the domain described in Fig. 2.3 up to to a time of 8×10^6 s using time steps $\Delta t = \{2 \times 10^5\,\text{s}, 1 \times 10^5\,\text{s}, 8 \times 10^4\,\text{s}, 5 \times 10^4\,\text{s}, 2.5 \times 10^4\,\text{s}\}$. For the convergence study, a relative error in mass loss was defined as

$$e_{ml}(\Delta t) = \frac{|M_l(\Delta t) - M_l(\Delta t_r)|}{|M_l(\Delta t_r)|} \tag{2.40}$$

where $M_l(\Delta t)$ is the total mass obtained by integrating Eq. (2.32) over time and space using a time step Δt and $M_l(\Delta t_r)$ is the mass loss computed using a reference time step that correspond to the "most accurate" solution available. For this example, we used $\Delta t_r = 2.5 \times 10^4$ s. Fig. 2.4 shows a plot of the relative error e_{ml} versus the inverse of time step. The time axis has been normalized so that Δt_r has a value of 1 on the $1/\Delta t$ axis. We can observe form this figure that the relative error decreases monotonically with decreasing time step, which indicates that the mass loss is converging towards a value.

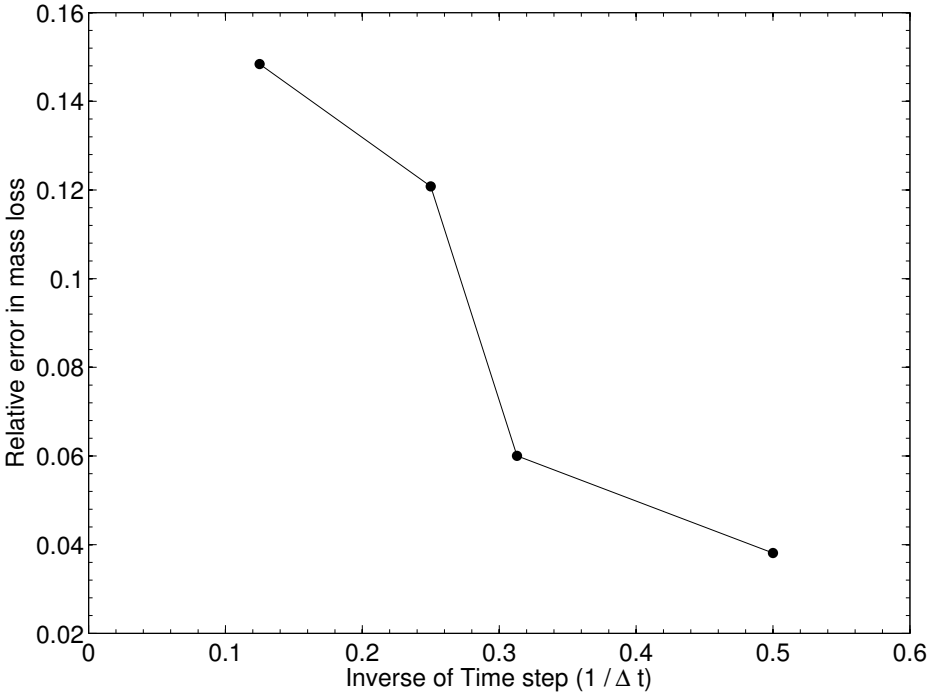

Figure 2.4: Relative error in total dissolved mass computed using different time steps.

As discussed in Section 2.3.3, the anode-cathode distribution evolves during the process of corrosion. It is important to modify the anodic and cathodic boundaries accurately at each time as these boundaries affect the distribution

and magnitude of the corrosion current. Hence, we studied how our proposed methodology captured the evolution of the ratio of anode area to cathode area (anode-cathode ratio) with time. Fig. (2.5) shows the anode-cathode ratio versus time for simulations using different time steps. For the time steps 2×10^5 s and 10^5 s it is difficult to claim an increasing or a decreasing trend in the anode-cathode ratio. This behavior was due to the coarseness of these time steps and the corresponding large errors in the numerical integration. However, it can be seen that for smaller time steps the anode-cathode ratio steadily decreased with time. This behavior was expected for the material domain illustrated in Fig. (2.3) as, once exposed, the vertical walls of the grain boundary can act as cathodic boundaries. Since the anodic area remains almost constant, there is a monotonic decrease in the anode-cathode ratio over time. Moreover, we observe in Fig. (2.3) that the anode-cathode ratio curves get closer to each other as the time step decreased, displaying a convergent behavior.

We also explored the sensitivity of the total corrosion current to the anode-cathode ratio. The total corrosion current was obtained as an integral of the current density over the anode at every time step. The results presented next were obtained using a time step $\Delta t = 2.5 \times 10^4$ s, which was deemed adequate to produce accurate results as determined from our convergence studies. Fig. (2.6) shows plots of the anode-cathode ratio and the evolution of the total corrosion current. For comparison purposes, the values of the corrosion current and anode-cathode ratio were normalized by dividing by their respective values at time $t = 0$.

In Fig. (2.6), we observe that the anode-cathode ratio decreased with time almost linearly, while the total corrosion current increased monotonically. This

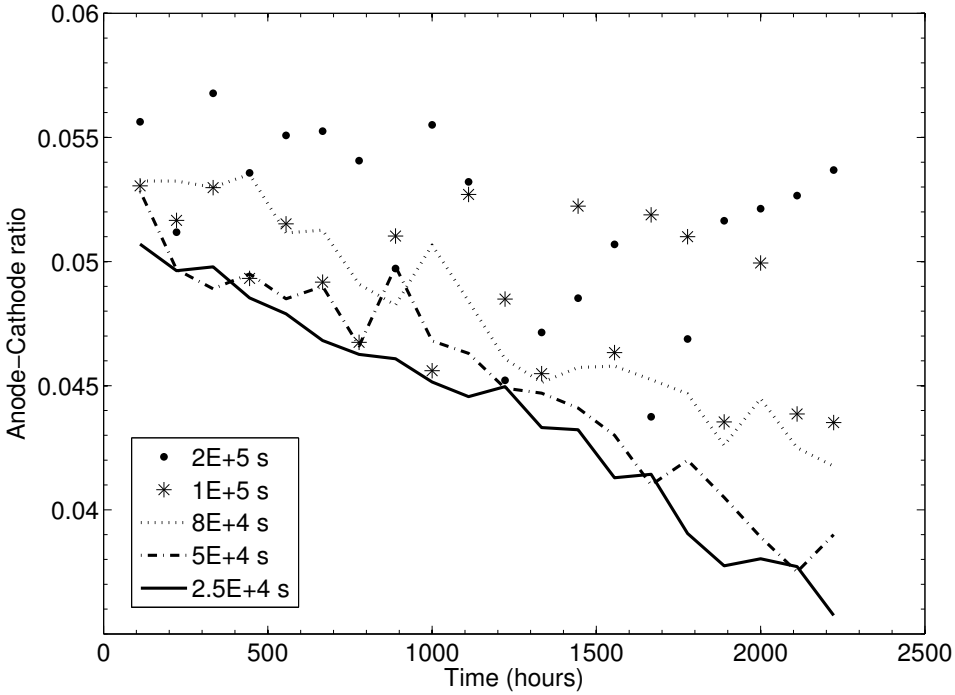

Figure 2.5: Anode-cathode ratio evolution with various time steps.

result can be explained by noticing that as the anode-cathode ratio decreases, the current density is expected to increase, and since the anode area remained nearly constant in this example, the total current increases with time. The increase in current density as the anode-cathode ratio decreased is confirmed by the plot of current density versus time shown in Fig. (2.7).

We notice that the trends of the total current and the current density shown in Figs. (2.6) and (2.7) are similar. Therefore, for this particular example, a higher magnitude of the total corrosion current implies a higher penetration rate, which is proportional to the current density.

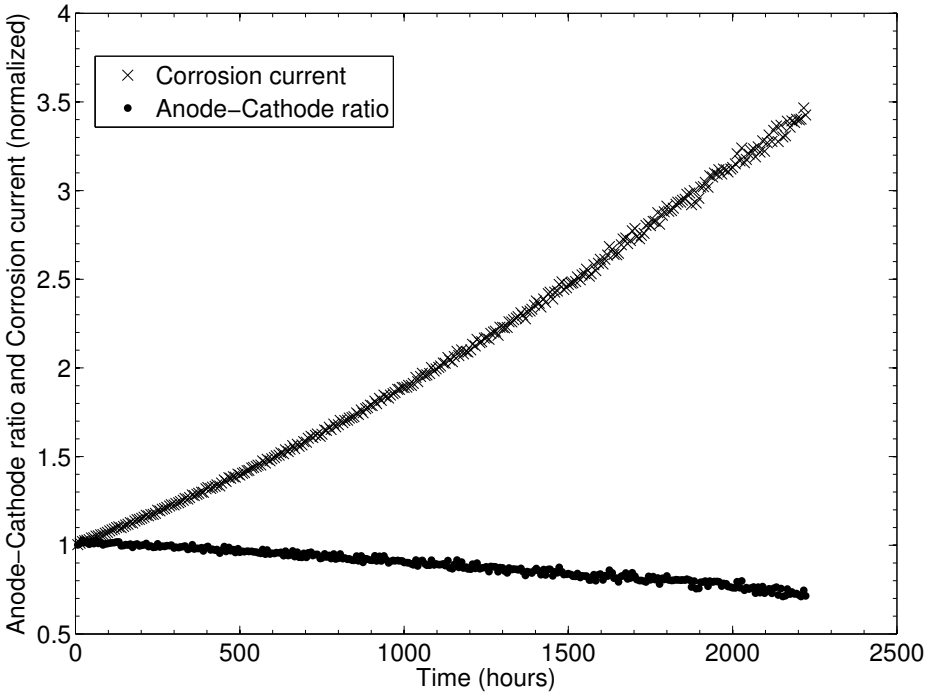

Figure 2.6: Anode-cathode ratio and total corrosion current for Example 1.

2.4.2 Example 2: Anodic inclusion

The purpose of this example is to study the behavior of an alloy-electrolyte system in which both the total anodic area and the the anode-cathode ratio change with time. We used the same electrolyte domain as in the previous example, but with a different geometric configuration for the alloy. We defined an arbitrarily shaped anodic inclusion inside a cathodic grain. A sketch of the system and the corresponding finite element mesh are shown in Fig. (2.8). In this case, dissolution is simulated until the entire anodic region was consumed due to corrosion.

Fig. (2.9) shows the evolution of the anode-cathode ratio and the total corrosion current over time. As in the previous example, these quantities were

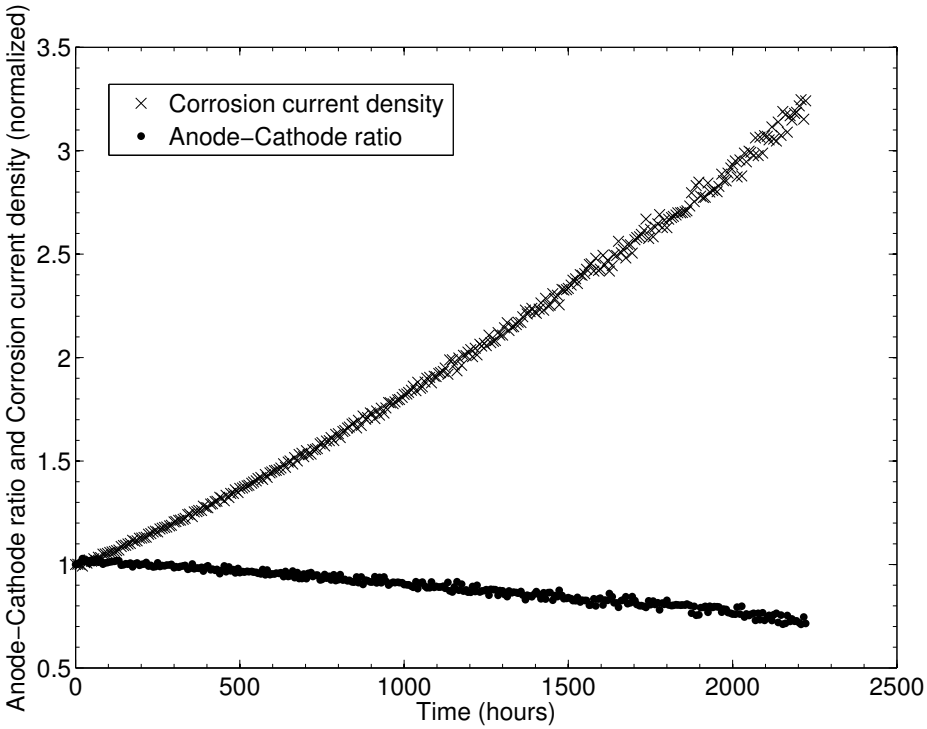

Figure 2.7: Anode-Cathode ratio and corrosion current density for Example 1.

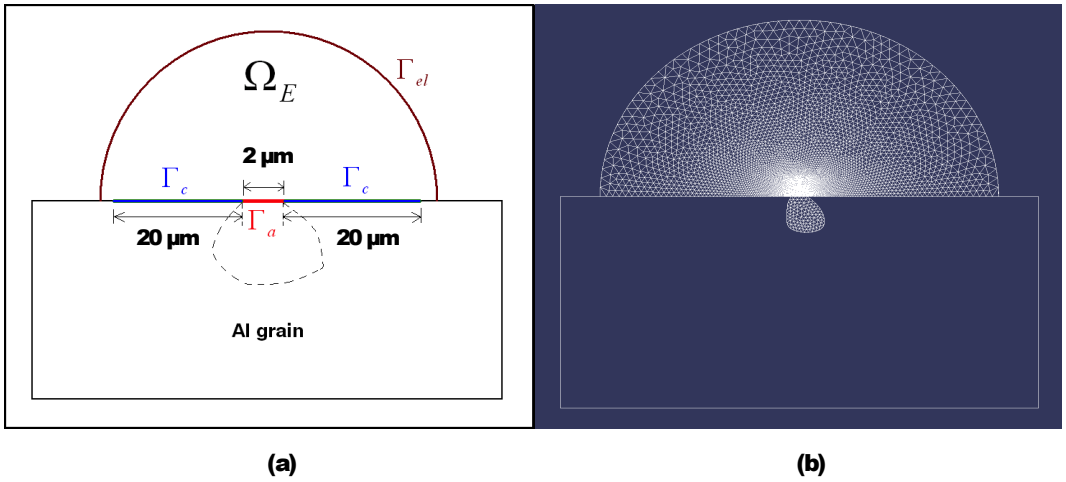

Figure 2.8: (a) Domain for Example 2. (b) Corresponding finite element mesh.

normalized with respect to their values at $t = 0$.

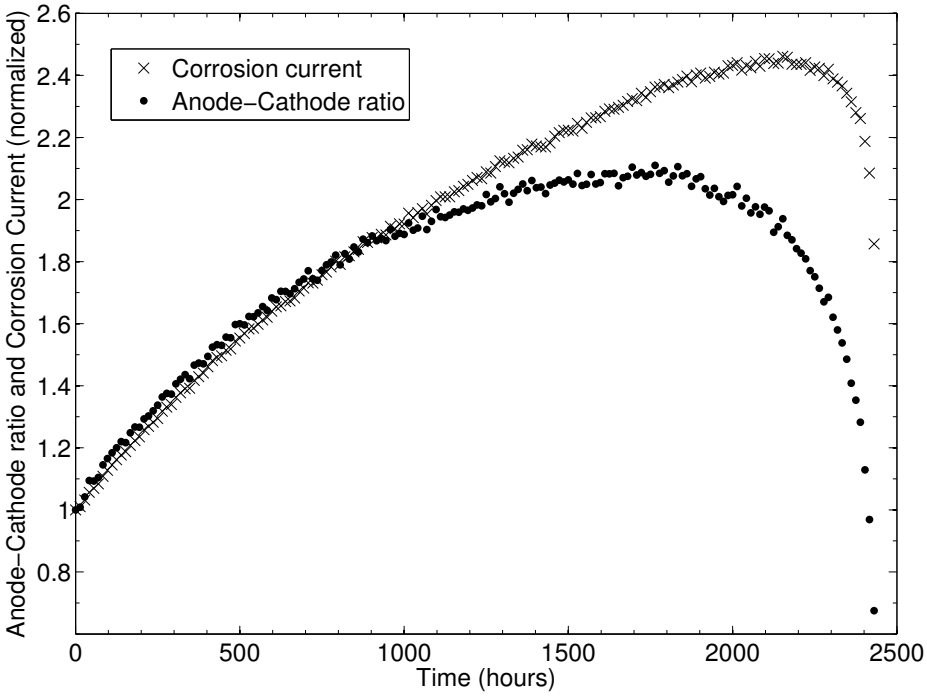

Figure 2.9: Anode-cathode ratio and total corrosion current for Example 2.

It is observed from Fig. (2.9) that both the anode-cathode ratio and the total corrosion current increased steadily to a maximum value, and then decayed to zero as the anodic region was completed dissolved. Furthermore, Fig. (2.10) shows that the current density decreased slightly and stayed nearly constant until the anode-cathode ratio reached its maximum value, and then increased sharply as the anode-cathode ratio decreased to zero. The system behavior shown in Figs. (2.9) and (2.10) can be explained by considering two competing factors. First, the increase in the anode-cathode ratio leads to a decrease of the corrosion current density. Second, an increase in the total anodic area yields an increase in the total current.

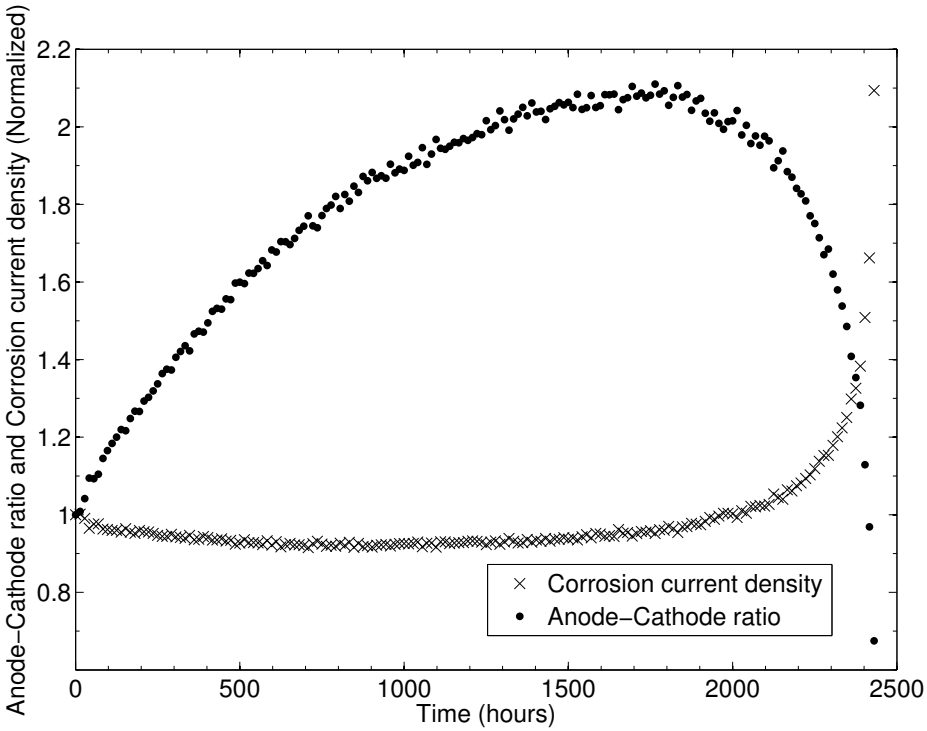

Figure 2.10: Anode-cathode ratio and corrosion current density for Example 2.

For this particular example, it appears that the second factor dominated the evolution of the total current (until a maximum was reached) as we observed a growth in the total corrosion current with time. It is interesting to notice that, unlike the previous example where an increase in corrosion current corresponded to a higher penetration rate, in this example the penetration rate remained almost constant during most of the corrosion process even though the total current was increasing.

It is important to notice how the geometric changes in the alloy domain affect the concentration of ionic species at the anodic surface. Fig. (2.11) shows a plot of the evolution of the average concentration of Mg^{2+} at Γ_a for both of the examples considered in this paper. Notice that the concentration (normalized

with respect to the values at $t = 0$) of Mg^{2+} increased much faster for the system studied in Example 1 than for that of Example 2, which is in agreement with the evolution of the current density in each case. As the current density is proportional to production of Mg^{2+} per unit area, the rate of accumulation for the ionic species is, as expected, higher for the domain shown in Fig. (2.3) than for the domain shown in Fig. (2.8).

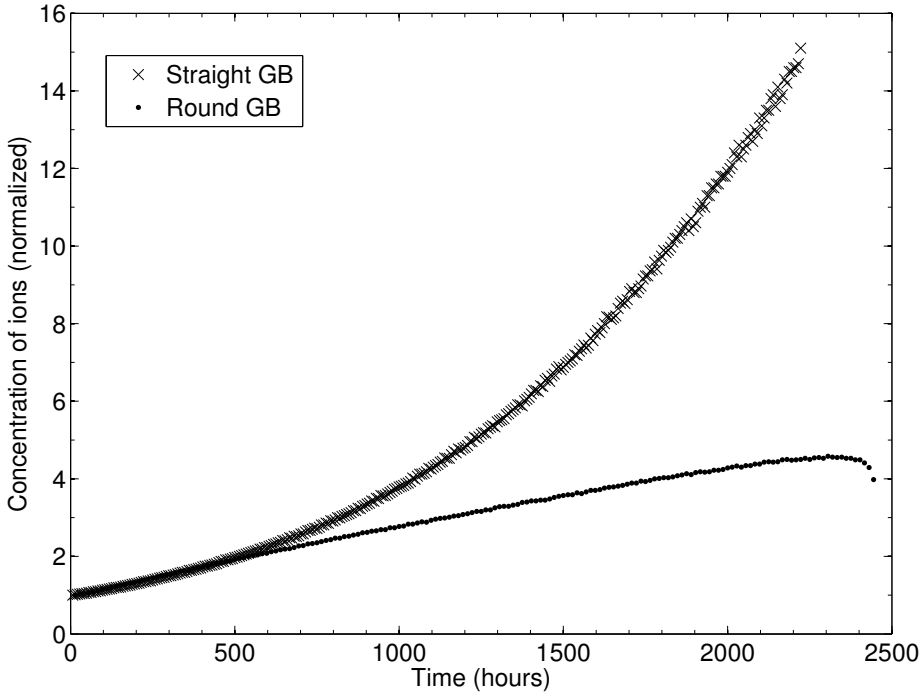

Figure 2.11: Evolution of Mg^{2+} concentration over the anodic surface.

We should mention that geometric organization of the alloy grain-grain boundaries is not the only factor determining the evolution of the anode-cathode ratio. Changes in the chemical environment also influences the favorability of the anodic or the cathodic reactions. Also, formation and deposition of corrosion products on the alloy surface will also affect corrosion current and the evolution of the anode-cathode ratio. Our current formulation does not include

these additional processes, which will be pursued in future work.

We conclude this section by showing in Fig. (2.12) the evolution of the anode-cathode boundary for the second example.

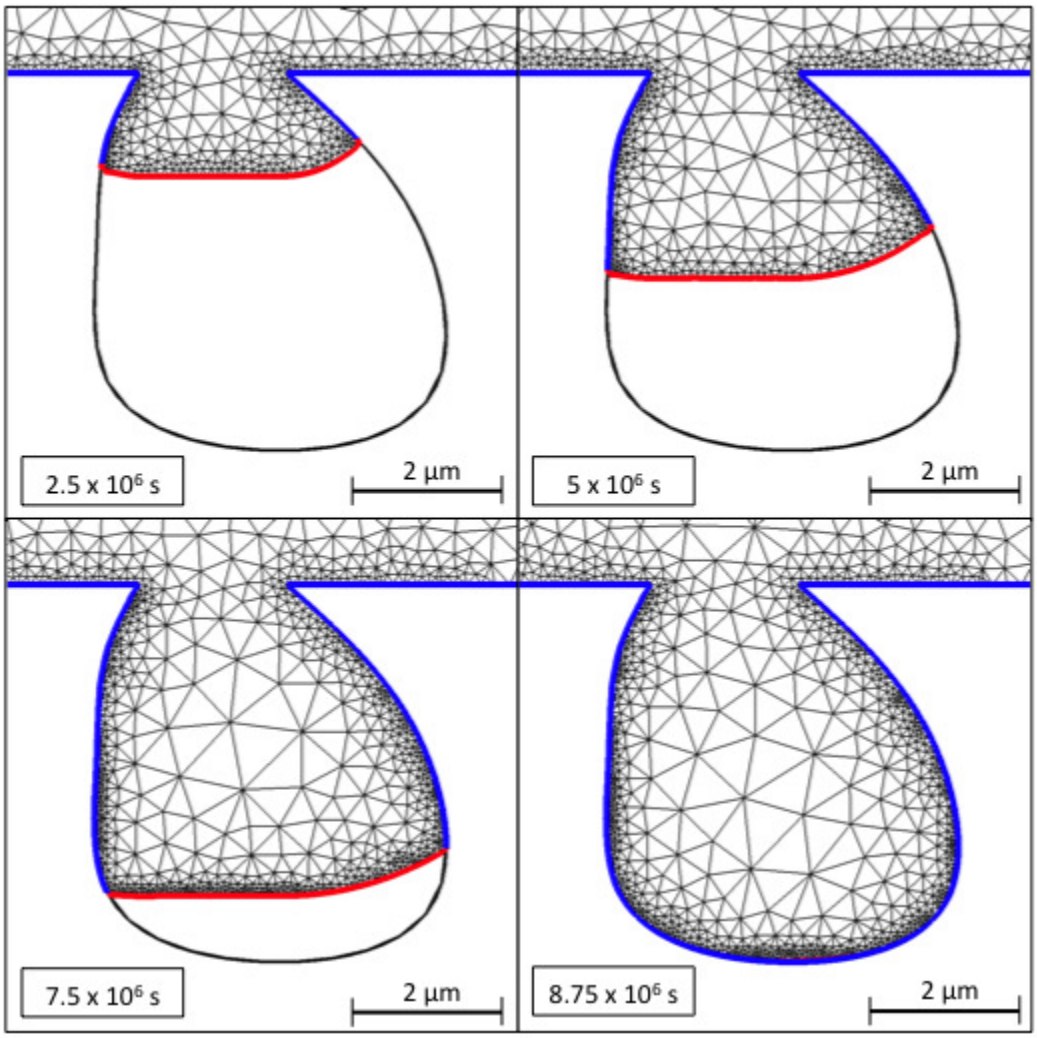

Figure 2.12: Changing anodic-cathodic boundary for Example 2.

This figure shows snapshots of the position of the anodic front at different times, where it can be seen how the finite element mesh is adapted as the geometry of the alloy-electrolyte system changes.

2.5 Concluding Remarks

We presented a computational framework for simulating corrosive dissolution over large periods of time. In our proposed approach the current density is computed from coupled transport equations and Gauss' law. Then, using conservation of mass, Faraday's law, and Reynold's transport theorem, we derived an equation of motion for the anodic front in terms of the current density. The finite element method, along with an adaptive meshing strategy, was used to compute the evolution of the ionic fields, current density, and movement of the anodic front. We demonstrated the capabilities of the proposed approach through two numerical examples that showed the dynamics of a corroding system in the presence of a moving anodic front. In these examples, we were able to confirm that the proposed framework displayed convergence for integral quantities, such as mass loss, total current, and current density as time steps were reduced. Although the grain-grain boundary composition is not the only factor that effect the evolution of the anodic and the cathodic boundaries, our proposed framework can be useful in determining the extent to which different microstructures are susceptible to corrosion. Our examples demonstrated that our proposed mathematical/numerical framework can capture the complex dynamics that ensures from the full coupling between anodic dissolution, ionic transport, and electric potential distribution.

2.6 Acknowledgements

We express our gratitude to the National Science Foundation for the financial support for this project through Award #CAREER-0643618. We would also like

to thank the Cornell Fracture Group for providing us with their C++ routines used for adaptive re-meshing in the proposed framework.

Bibliography

[1] D.R. Baer, C.F. Windisch, M.H. Engelhard, M.J. Danielson, R.H. Jones, and J.S. Vetrano. Influence of mg on the corrosion of al. *Journal of Vacuum Science & Technology A: Vacuum, Surfaces, and Films*, 18(1):131–136, 2000.

[2] T. Belytschko, W. K. Liu, and B. Moran. *Nonlinear finite elements for continua and structures*. Wiley New York, 1st edition, 2006.

[3] K. Bhargava, A.K. Ghosh, Y. Mori, and S. Ramanujam. Model for cover cracking due to rebar corrosion in rc structures. *Engineering Structures*, 28(8):1093–1109, 2006.

[4] J.O.M. Bockris and A.K.N. Reddy. *Modern Electrochemistry*. Springer, 2nd edition, 1998.

[5] R.P. Buck. Kinetics of bulk and interfacial ionic motion: microscopic bases and limits for the nernstplanck equation applied to membrane systems. *Journal of Membrane Science*, 17(1):1–62, 1984.

[6] P.J. Mucha C. Wojtan, M. Carlson and G. Turk. Animating corrosion and erosion. In *Eurographics Workshop on Natural Phenomena*, pages 21–29. Citeseer, 2007.

[7] J.C. Chang and T.H. Chuang. The degradation of corrosion resistance for al 5083 alloy after thermal and superplastic forming processes. *Journal of Materials Engineering and Performance*, 9(3):253–260, 2000.

[8] C. Dan, B. Van den Bossche, L. Bortels, G. Nelissen, and J. Deconinck. Numerical simulation of transient current responses in diluted electrochemical ionic systems. *Journal of Electroanalytical Chemistry*, 505(1):12–23, 2001.

[9] L.C. Evans. *Partial differential equations*. AMS, 1st edition, 2008.

[10] S. Gavrilov, M. Vankeerberghen, G. Nelissen, and J. Deconinck. Finite element calculation of crack propagation in type 304 stainless steel in diluted sulphuric acid solutions. *Corrosion Science*, 49(3):980–999, 2007.

[11] C.W. Gear and I.G. Kevrekidis. Projective methods for stiff differential equations: problems with gaps in their eigenvalue spectrum. *SIAM Journal on Scientific Computing*, 24(4):1091–1106, 2003.

[12] K. Hebert and R.C. Alkire. Dissolved metal species mechanism for initiation of crevice corrosion of aluminum ii. mathematical model. *Journal of the Electrochemical Society*, 130(5):1007–1014, 1983.

[13] D.A. Jones. *Principles and prevention of corrosion*. Prentice Hall, 2nd edition, 1996.

[14] G.F. Kennell, R.W. Evitts, and K.L. Heppner. A critical crevice solution and ir drop crevice corrosion model. *Corrosion Science*, 50(6):1716–1725, 2008.

[15] I.G. Kevrekidis, C.W. Gear, and G. Hummer. Equation-free: The computer-aided analysis of complex multiscale systems. *AIChE Journal*, 50(7):1346–1355, 2004.

[16] A. King, G. Johnson, D. Engelberg, W. Ludwig, and J. Marrow. Observations of intergranular stress corrosion cracking in a grain-mapped polycrystal. *Science*, 321(5887):382–385, 2008.

[17] S.C. Kranc and A.A. Sagüés. Detailed modeling of corrosion macrocells on steel reinforcing in concrete. *Corrosion Science*, 43(7):1355–1372, 2001.

[18] E. Kuş and F. Mansfeld. An evaluation of the electrochemical frequency modulation (efm) technique. *Corrosion Science*, 48(4):965–979, 2006.

[19] C.M. Liao and R.P. Wei. Galvanic coupling of model alloys to aluminuma foundation for understanding particle-induced pitting in aluminum alloys. *Electrochimica Acta*, 45(6):881–888, 1999.

[20] J. Newman and K.E. Thomas-Aleya. *Electrochemical Systems*. Prentice-Hall, 3rd edition, 2004.

[21] Y. Onishi, J. Takiyasu, K. Amaya, H. Yakuwa, and K. Hayabusa. Numerical method for time-dependent localized corrosion analysis with moving boundaries by combining the finite volume method and voxel method. *Corrosion Science*, 2012.

[22] L. Onsager. Reciprocal relations in irreversible processes. i. *Physical Review*, 37(4):405, 1931.

[23] R.M. Pidaparti, M.J. Palakal, and L. Fang. Cellular automation approach to model aircraft corrosion pit damage growth. *AIAA Journal*, 42(12):2562–2569, 2004.

[24] S. Sarkar and W. Aquino. Electroneutrality and ionic interactions in the modeling of mass transport in dilute electrochemical systems. *Electrochimica Acta*, 56(24):8969–8978, 2011.

[25] S.M. Sharland. A mathematical model of the initiation of crevice corrosion in metals. *Corrosion Science*, 33(2):183–201, 1992.

[26] W. Sun and K.M. Liu. Numerical solution of cathodic protection systems with nonlinear polarization curves. *Journal of The Electrochemical Society*, 147(10):3687–3690, 2000.

[27] M. Vankeerberghen, S. Gavrilov, and G. Nelissen. Finite element calculation of the polarisation behaviour of a metal in an aqueous solution using the dilute solution model. *Corrosion Science*, 43(1):37–51, 2001.

[28] R.P. Wei. A model for particle-induced pit growth in aluminum alloys. *Scripta Materialia*, 44(11):2647–2652, 2001.

[29] L. Yuan-Hui and S. Gregory. Diffusion of ions in sea water and in deep-sea sediments. *Geochimica et Cosmochimica Acta*, 38(5):703–714, 1974.

CHAPTER 3

MODIFICATIONS IN THE ELECTRODIC REACTION RATES DUE TO STRESS AND STRESS-INDUCED SURFACE PATTERNS

We present a stress and surface-curvature dependent model for electrode kinetics. Based on our calculations we establish that depending upon the material properties it is possible to considerably change electrodic reaction rates using stress. We used a curvature-sensitive surface tension to calculate the effect of surface patterns. On evaluating the effect of surface patterns with high wavenumbers we obtained large shifts in the reaction rate due to surface tension. The periodic stress field created due to the surface patterns was found to produce additional changes in the reaction rate. We also demonstrated the motion of an anodic dissolution front using stress-coupled dissolution and established the change in the shape and the reaction rate caused due to the stress.

3.1 Introduction

Electrodic reactions are a fundamental component of physical processes like corrosion, electrodeposition, fuel cells, and batteries. A model for electrodic reactions is required to estimate essential engineering quantities, like electric power (as in fuel cells), and life of metal structures (as in corrosion). Most of the electrodic reactions are assumed to operate under constant pressure [14, 2, 15]. However, a stress field could be present in an electrodic domain due to the functional design, as in corrosion [15], or it could be due to the accumulation of reaction products, as in power generating electrodes [11, 6]. Also, stress-induced

S. Sarkar and Wilkins Aquino, Modifications in the electrodic reaction rates due to stress and stress-induced surface patterns, to be submitted.

surface instabilities [5, 23], can change the electrode chemical potential [3, 22], and subsequently alter the reaction rate.

Though the use of stress-dependent chemical potential has been well-known in the evolution of surface morphology [18, 21], electrodic reaction rates, specifically corrosion rates, are generally modeled using a stress-independent Butler-Volmer equation [14, 2]. The advantage of a stress-coupled model for electrodic reactions is two fold: This type of model would extend the use of experimentally measured electrodic quantities beyond the stress level of the experimental setup, and allow us to manipulate the rate of electrodic reactions by the application of stress.

In our work, electrode kinetics was determined by a stress-dependent chemical potential using the Gibbs-Duhem equation [16, 7]. Using the existing theories of curvature-dependent chemical potential [23, 3, 22, 27, 25, 10] and surface tension [24, 17] we also established the change in the macroscopic electrodic reaction rate due to the formation of micron and sub-micron size surface patterns. Our calculations show that we can use stress to extract a wider range of reaction rates from the same electrode-electrolyte combination. We observed that depending upon the amplitude and the wavelength of the stress-induced surface patterns we can further modulate the reaction rate. We also demonstrate that the motion of an anodic front due to stress-coupled dissolution is sensitive to the magnitude of the stress and the mechanical boundary condition on the electrode. There exists other processes, for example rupture of passive layer due to dislocations [8], repassivation, and hydrogen adsorption, which can also effect the electrodic reaction rate. However, our aim in this paper is to determine the contribution of reversible stress fields and morphological changes on

the surface.

3.2 Background

Let the reaction across an alloy-electrolyte interface be

$$R_s \rightleftharpoons O_s^{n+} + ne^-$$

where R_s is the reduced state of a species s, O_s^{n+} is the oxidized state, and n is the number of electrons exchanged. Hence, the change in free energy due to the electron transfer from the electrolyte to the alloy is

$$\Delta G = \mu_{R_s} - \mu_{O_s^{n+}} \tag{3.1}$$

where μ_{R_s} and $\mu_{O_s^{n+}}$ are the chemical potentials. The net reaction rate [2, 12] due to ΔG is given as

$$i = i_0\Big[\exp\Big(-\frac{(1-\alpha)(\Delta G - \Delta G_0)}{RT}\Big) - \exp\Big(\frac{\alpha(\Delta G - \Delta G_0)}{RT}\Big)\Big] \tag{3.2}$$

where ΔG_0 is the open-circuit free energy barrier, i_0 is the open-circuit current density, α is the transfer coefficient, R is the gas constant, and T is the temperature. The free energy barrier is related to the electrode potential ϕ as $\Delta G = -nF\phi$ [15, 12], where F is Faraday's constant.

Now, in the event of any mechanical deformation in the alloy domain, there is a shift in the chemical potential of R_s, $\Delta\mu_{R_s}$. Correspondingly, the modified free energy barrier $\Delta\tilde{G}$ will be

$$\Delta\tilde{G} = \mu_{R_s} + \Delta\mu_{R_s} - \mu_{O_s^{n+}} \tag{3.3}$$

Substituting Eq. (3.3) into Eq. (3.2), and factoring out the contribution due to the open-circuit potential, we obtain the modified rate equation as

$$i = i_0\left[\exp\left\{-\frac{(1-\alpha)}{RT}\Delta\mu_{\mathrm{R_s}}\right\}\exp\left(\frac{\eta}{\beta_f}\right) - \exp\left\{\frac{\alpha}{RT}\Delta\mu_{\mathrm{R_s}}\right\}\exp\left(\frac{\eta}{\beta_r}\right)\right] \tag{3.4}$$

where $\eta = \phi - \phi_0$, $\beta_f = \frac{RT}{(1-\alpha)nF}$, and $\beta_r = -\frac{RT}{\alpha nF}$. Eq. (3.4) shows that $\Delta\mu_{\mathrm{R_s}}$ will produce an extra factor in the forward and the reverse reaction rates.

3.3 Stress-induced changes in electrodic reaction rates

The shift $\Delta\mu_{\mathrm{R_x}}$ is determined with respect to a reference state. This reference state is a stress-free electrode with a zero curvature surface. Mechanical loading of the electrode creates a stress field, and it may also cause surface instabilities. In Fig. 3.1 we have illustrated the reference and the modified electrodic surfaces.

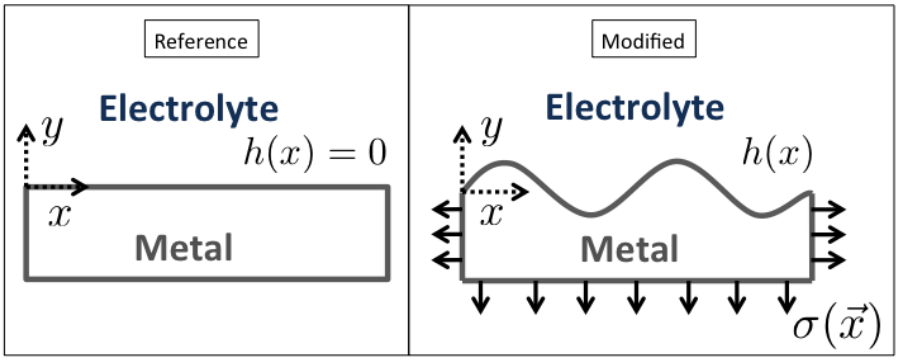

Figure 3.1: Reference and modified configurations for the electrode surface.

3.3.1 Direct Effect of stress

As the first step, we determine the modified reaction rate (3.4) only due to the stress field, while assuming the surface profile to be unchanged. According to Gibbs-Duhem equation [16], differentials of the thermodynamic potentials are related as

$$N d\mu = V dP - S\, dT \tag{3.5}$$

We will use the following additional assumptions

1. N = 1 and V is the atomic volume $\Omega_{\mathrm{R_s}}$.
2. The stress field over $\Omega_{\mathrm{R_s}}$ is uniform.
3. The material response is linearly elastic.
4. $dT = 0$ during mechanical loading.

Using the above conditions, we integrate Eq. (3.5) from zero to the final stress level $\boldsymbol{\sigma}_f$ and obtain $\Delta\mu_{\mathrm{R_s}}$ as

$$\Delta\mu_{\mathrm{R_s}} = \int_0^{P(\boldsymbol{\sigma}_f)} \Omega_{\mathrm{R_s}}(\boldsymbol{\sigma})\, dP(\boldsymbol{\sigma}) \tag{3.6}$$

where the pressure $P(\boldsymbol{\sigma})$ is the negative of the hydrostatic component of $\boldsymbol{\sigma}$, to make it consistent with Eq. (3.5). Evaluating the integral in Eq. (3.6) we obtain

$$\Delta\mu_{\mathrm{R_s}} = \Omega_{\mathrm{R_s}}\left(P(\boldsymbol{\sigma}_f) - \frac{P(\boldsymbol{\sigma}_f)^2}{2K}\right) \tag{3.7}$$

where K is the bulk modulus. The contribution due to the strain energy density (2^{nd} term in Eq. (3.7)) is smaller than the 1st term by a factor of $P/2K$. For example, under uniaxial stress the value of $P/2K$ for Al at yield stress is $\approx 4.386\times 10^{-5}$. Hence, if we apply Eq. (3.7) in the regime of linear elasticity, then it is

reasonable to neglect the contribution of the 2^{nd} term to $\Delta\mu_{R_s}$ in comparison to $\Omega_{R_s}P$.

Substituting Eq. (3.7) into Eq. (3.4), we obtain

$$i = i_o\left[\exp\left(\xi_f P\right)\exp\left(\frac{\eta}{\beta_f}\right) - \exp\left(\xi_r P\right)\exp\left(\frac{\eta}{\beta_r}\right)\right] \tag{3.8}$$

where $\xi_f = -(1-\alpha)\Omega_{R_s}/(RT)$ and $\xi_r = \alpha\Omega_{R_s}/(RT)$. As $\xi_f < 0$ and $\xi_r > 0$, when the state of stress is tensile ($P < 0$), the anodic reaction rate is amplified and the cathodic reaction rate is diminished. Similarly, when $P > 0$ the anodic rate is diminished and the cathodic rate is amplified.

3.3.2 Effect of stress-induced surface curvature

Mechanical loading can also produce morphological changes at the surface. Two well-established mechanisms for such morphological changes are surface wrinkling [4], and surface diffusion [23]. The mechanism of formation of these patterns are described in the references. In our work we determine the change in the reaction rate once the patterns have been formed.

We will demonstrate our method for a 2D electrodic domain with a 1D electrode-electrolyte interface [3, 23]. The surface profile of a modified electrodic surface, as illustrated in Fig. 3.1, can be described as

$$h(x) = A\cos(\omega x) \tag{3.9}$$

where A is the amplitude and ω is the frequency.The surface curvature will create an additional shift in the chemical potential [3, 23]. The total value $\Delta\mu_{R_s}$ will be

$$\Delta\mu_{R_s}(x, h(x)) = \gamma\kappa(x)\Omega_{R_s} - \Omega_{R_s}\sigma_H(x, h(x)) \tag{3.10}$$

where σ_H is the hydrostatic stress, γ is the surface tension, and the curvature κ is defined [23] as

$$\kappa(x) = \frac{-h''(x)}{(1 + h'(x)^2)^{3/2}} \tag{3.11}$$

As shown by Tolman [24], surface tension also depends on the radius of curvature as

$$\gamma(\rho(x)) = \frac{\gamma_0}{1 + 2\delta/\rho(x)} \tag{3.12}$$

where $\rho(x)$ is the radius of curvature, γ_0 is the surface tension for $1/\rho = 0$, and δ is a material-dependent constant [24, 17, 13].

We will use the stress-field approximation by Asaro [3], which results in a $\sigma_H(x, h(x))$ as

$$\sigma_H(x, h(x)) = \sigma_H^0(1 - 2A\omega(\omega h(x) + 1)\exp(\omega h(x))\cos(\omega x)) \tag{3.13}$$

where σ_H^0 is the hydrostatic stress field inside the electrodic domain and away from the surface $h(x)$. $\sigma_H(x, h(x))$ along the surface could be zero if the alloy domain can be unloaded after the pattern formation. This may be possible for the patterns created by the irreversible process of surface diffusion.

Substituting equations (3.10) and (3.13) into Eq. (3.4), we obtain

$$\begin{aligned} i(x, h(x)) = i_o\Big[&\exp\Big\{\xi_f\gamma\kappa(x)\Big\}\exp\Big\{-\xi_f\sigma_H(x, h(x))\Big\}\exp\Big\{\frac{(1-\alpha)nF}{RT}\eta\Big\} \\ &- \exp\Big\{\xi_r\gamma\kappa(x)\Big\}\exp\Big\{-\xi_r\sigma_H(x, h(x))\Big\}\exp\Big\{-\frac{\alpha nF}{RT}\eta\Big\}\Big] \end{aligned} \tag{3.14}$$

where η is the overpotential before the stress-induced changes took effect. Since the patterns created by surface instabilities are periodic we can easily determine the macroscopic (or the average) change in the reaction rate. This average amplification-reduction factor for the forward component of the reaction rate is

$$\chi_{avg} = \frac{\omega}{\pi}\int_0^{\frac{\pi}{\omega}} \exp(\xi_f\gamma(x)\kappa(x)) - \xi_f\sigma_H(x, h(x)))\,dx \tag{3.15}$$

So, when we have a strong net reaction rate (*i.e.* the Butler-Volmer current is in the Tafel region), the stress-induced current density due to surface patterns is

$$i_{avg} = i_o \chi_{avg} \exp\left\{\frac{(1-\alpha)nF}{RT}\eta\right\} \tag{3.16}$$

Thus, we can compute the factor χ_{avg} and determine the influence of periodic patterns on the reaction rate.

3.4 Numerical Results and Discussion

We present three examples to show the amplification (or reduction) caused due to stress and stress-induced instabilities on the reaction rate. In all of our calculations we have assumed $\alpha = 0.5$ [15], and the $T = 300\,\mathrm{K}$.

3.4.1 Sensitivity to electrode material

Using Eq. (3.8), we calculated the change in the anodic dissolution rates for four different materials, Cu, CuBe, Al alloy AA 2014-T6, and high tensile strength steel A514. We selected these materials to show the extent to which we can change the reaction rate in different materials before yielding. The atomic volume of Al is $9.98\,\mathrm{cm^3 mol^{-1}}$, and for Cu and Fe it is $7.1\,\mathrm{cm^3 mol^{-1}}$. The uniaxial yield strength for the materials are listed in Table 3.1. In Fig. 3.2, we present the maximum amplification and reduction possible in the reaction rate for the four materials before yielding under uniaxial stress. The effect of stress on the anodic reaction rate for Cu electrode is negligible ($< 5\%$). However, for CuBe almost a 20 % increase in the anodic dissolution rate is possible. As the yield strength of

Electrode material	Yield strength (MPa)
Cu	70
CuBe	350
AA 2014-T6	414
A514 Steel	690

Table 3.1: Tensile yield strength for the materials.

A514 steel is much higher, we can obtain around 40 % increase under tension and almost a 30% decrease under compression. Though the yield strength of

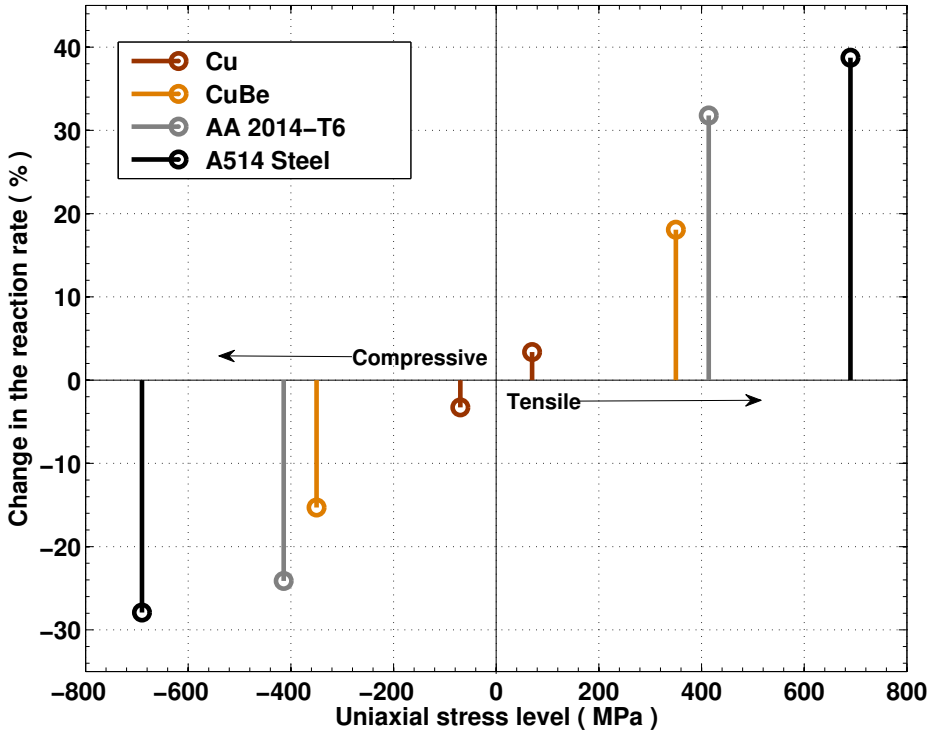

Figure 3.2: Maximum shift in the anodic rate for various materials within yield strength.

AA 2014-T6 is less than that of A514 by 276 MPa, we can cause almost a 35 % increase in the dissolution rate owing to the larger atomic volume of Al. Liu and

Frankel [20, 19] have experimentally observed the corrosion rates in stressed Al alloy specimens that agree in behavior with the results presented herein. So, the influence of stress on the corrosion rates of structural alloys can be significant.

3.4.2 Amplification-Reduction due to curvature

We calculated χ_{avg} (3.15) for a range of amplitudes A and wavelengths λ ($= \frac{2\pi}{\omega}$). The atomic volume used for this example was $10\,\mathrm{cm^3 mol^{-1}}$. Surface tension for the flat surface (*i.e.* γ_0) was assumed to be $1.25\,\mathrm{Nm^{-1}}$ (a value for Al [13]). We used a reported value of $\delta = 2.5$ [1], and we obtained a similar estimate for it using the method by Jiang [13].

Fig. **??** shows χ_{avg} (3.15) for $A = 0.1\,\mu\mathrm{m}$ to $1\,\mathrm{nm}$ and $\lambda = 0.5\,\mu\mathrm{m}$ to $5\,\mathrm{nm}$. Based on the reported dimensions of patterns [26] we have only evaluated for $A\omega < 1.5$. Fig. **??** shows the same plot when $\delta = 0$. For $\delta = 2.5$ we obtain an average amplification by a factor of 2, which further increased to 9 for $\delta = 0$. From Fig. 3.3, we can state that the shift in the reaction rate due to the surface tension can be important at high wavenumbers, and the effect increases upon decreasing the value of δ.

In Fig. 3.4 we plot χ_{avg} under the combined influence of γ and stress for $A = 10\,\mu\mathrm{m}$ to $1\,\mathrm{nm}$ and $\lambda = 50\,\mu\mathrm{m}$ to $5\,\mathrm{nm}$. As Asaro's solution (3.13) is a better approximation when $A\omega$ is small [3], we have only calculated χ_{avg} when $A\omega < 0.6$ [9]. As the stress contributing to the surface instabilities is generally compressive [4] we have used $\sigma_H^0 = \{-50, -300\}\,\mathrm{MPa}$. From Fig. 3.4, our first observation is that, when A is much smaller than λ (*i.e.* near the $(-3, -0.5)$ corner) the reaction rate is diminished (as expected due to compression). However, when A

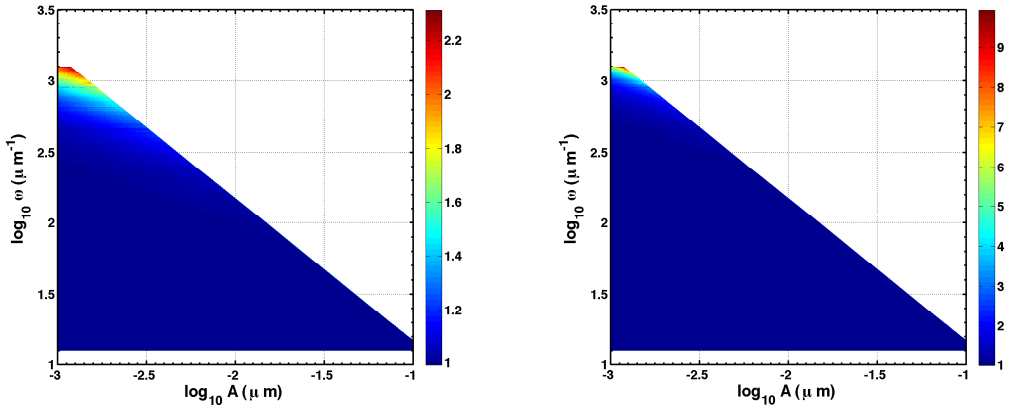

(a) $\delta = 2.5$ (b) $\delta = 0$

Figure 3.3: Curvature-dependent amplification χ_{avg} when $\sigma_H^0 = 0$.

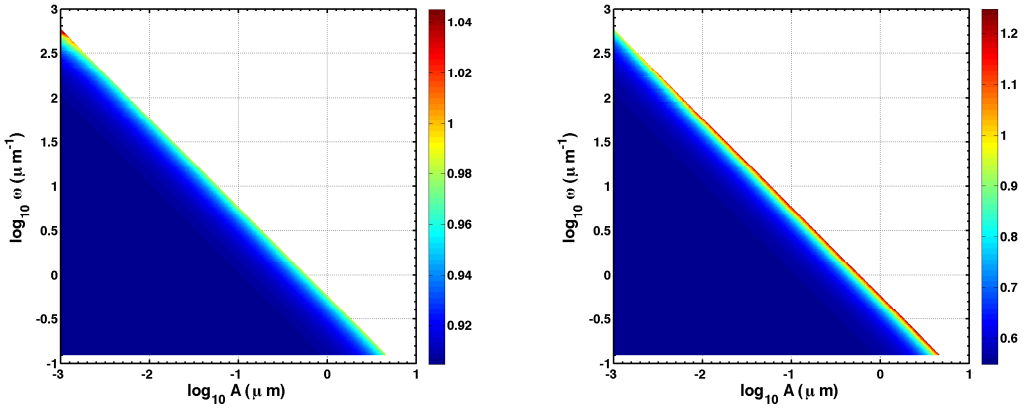

(a) $\sigma_H^0 = -50\,\text{MPa}$ (b) $\sigma_H^0 = -300\,\text{MPa}$

Figure 3.4: Curvature-dependent amplification χ_{avg} in the presence of stress.

and λ are comparable (*i.e.* along the diagonal of the plots), the periodic σ_H can cause an increase in the reaction rate. At $\sigma_H^0 = -300\,\text{MPa}$ it is possible to alter the rate within $(-50\%, +20\%)$ by using surface patterns. So, stress-induced surface patterns may become useful in modulating the reaction rates.

3.4.3 Effect of stress-coupled reaction on the shape of dissolution fronts

We consider a plate with a circular hole, as shown in Fig. 3.5, loaded along the Y direction with $\sigma > 0$. We assume that without stress the boundary of the hole, Γ_{corr}, is undergoing uniform dissolution. Thus, increasing the radius with time

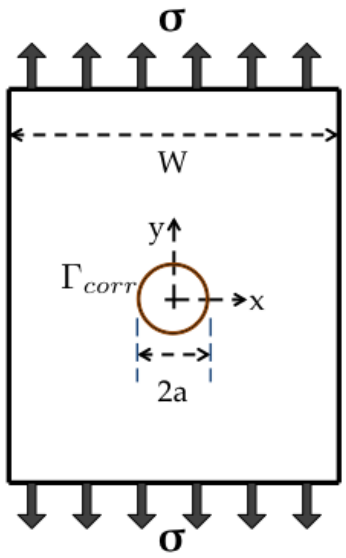

Figure 3.5: Plate with a circular hole under uniaxial tensile stress

without any change in shape. Assuming $a/W \ll 1$, the solution to the stress field is known due to Inglis. Specifically, the stress field causes

$$\sigma_{yy}(t) = \sigma\left(1 + 2\sqrt{\frac{a(t)}{\rho(t)}}\right) \quad \text{at } (\pm a(t), 0) \tag{3.17}$$

and

$$\sigma_{xx} = -\sigma \quad \text{at } (0, \pm b(t)) \tag{3.18}$$

where $\rho(t)$ is the radius of the curvature at $(\pm a(t), 0)$, and initially $a(0) = b(0) = \rho(0)$.

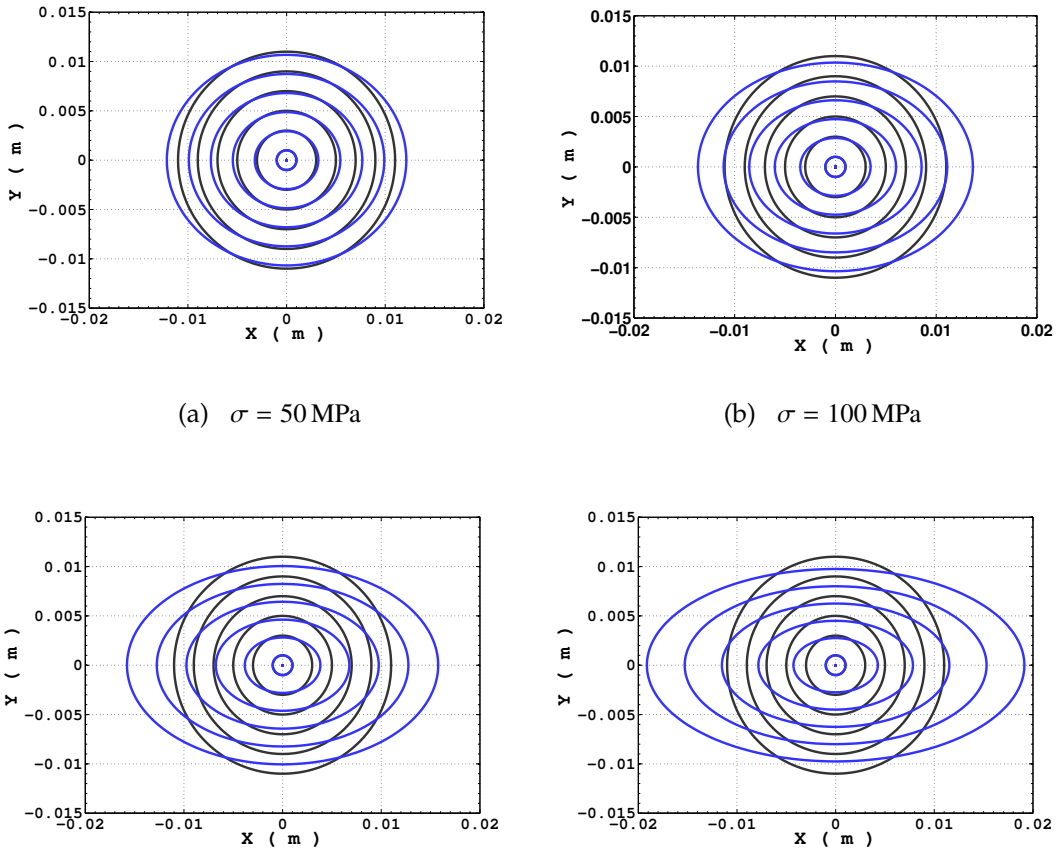

(a) $\sigma = 50\,\text{MPa}$ (b) $\sigma = 100\,\text{MPa}$

(c) $\sigma = 150\,\text{MPa}$ (d) $\sigma = 200\,\text{MPa}$

Figure 3.6: Evolution of a circular hole under stress-free and stress-coupled dissolution.

The evolution of the circular hole both for stress-free and stress-coupled anodic dissolution is shown in Fig. 3.6, for $a(0) = 1\,\text{mm}$, and a stress-free dissolution rate of $r = 1\,\mu\text{ms}^{-1}$. The total period of simulation was $[0, 10^4\,\text{s}]$ with a time step of 0.1 s. The location of the dissolution front is displayed after every 2×10^4 time steps. The black contours show stress-free dissolution and the blue lines show stress-coupled dissolution. For each of the stress levels, we observe that stress-coupled dissolution increases the ellipticity of the hole. Moreover, the rate of change in ellipticity increases with the magnitude of tensile stress.

As evident from Eq. (3.17), an increase in ellipticity leads to an increase in the tensile stress at the ends of the major axis. Thus, amplifying the local dissolution rate even more.

In Fig. 3.7, we present the total mass loss rate across Γ_{corr}. The cumulative effect of the stress field at Γ_{core} for this problem is an increase in the total dissolution rate. Increasing σ we obtain a faster increase the total dissolution rate. This example establishes that the evolution of both the shape and the rate of

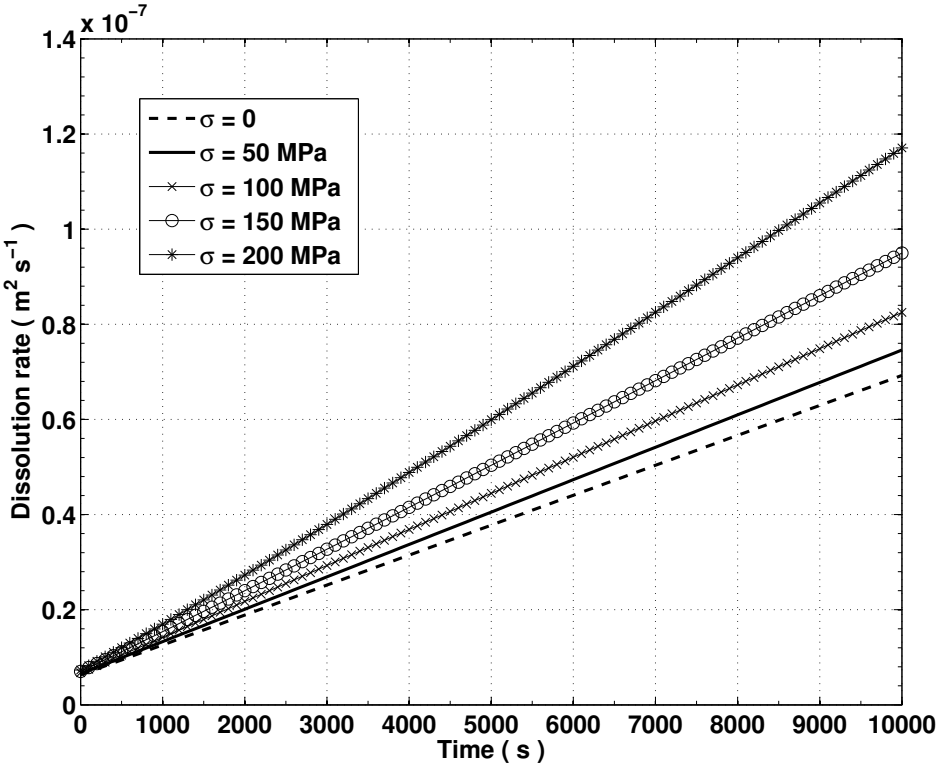

Figure 3.7: Evolution of the total dissolution rate across Γ_{corr}.

dissolution of an anodic front is strongly sensitive to the stress field generated by the mechanical loading of the electrode domain.

3.5 Conclusion

A method to determine stress-induced changes in the electrodic reaction rates was presented. The increase in the reaction rate due to stress could be high for structural alloys undergoing corrosion. At high wavenumber surface patterns the reaction rate can change considerably depending on the surface tension. Though the change due to surface tension is only prominent at high wavenumbers, the effect due to a periodic stress field is large whenever the amplitude and the wavelength are of similar dimensions. The development of surface patterns is a highly active experimental research field, and our calculations show that these patterns could be useful for electrochemical purposes. As demonstrated using the last example we can also use stress-coupled reaction with suitable mechanical boundary conditions on the electrode to manipulate the motion of an electro-dissolution or electrodeposition front.

3.6 Acknowledgment

We are grateful for the generous support of the National Science Foundation through Award #CAREER-0643618 that enabled this work.

Bibliography

[1] A. W. Adamson and A. P. Gast. *Physical Chemistry of Surfaces*. Wiley-Interscience, 6th edition, 1997.

[2] L.R. Faulkner A.J. Bard. *Electrochemical Methods: Fundamentals and Applications*. Wiley, 2nd edition, 2000.

[3] R. Asaro and W. Tiller. Interface morphology development during stress corrosion cracking: Part i. via surface diffusion. *Metallurgical and Materials Transactions B*, 3:1789–1796, 1972.

[4] N. Bowden, S. Brittain, A. G. Evans, J. W. Hutchinson, and G. W. Whitesides. Spontaneous formation of ordered structures in thin films of metals supported on an elastomeric polymer. *Nature*, 393(6681):146–149, 1998.

[5] X. Chen and J. W. Hutchinson. Herringbone buckling patterns of compressed thin films on compliant substrates. *Journal of Applied Mechanics*, 70:597 – 603, 2004.

[6] Yang-Tse Cheng and Mark W. Verbrugge. Evolution of stress within a spherical insertion electrode particle under potentiostatic and galvanostatic operation. *Journal of Power Sources*, 190(2):453 – 460, 2009.

[7] K. A. Dill and S. Bromberg. *Molecular Driving Forces: Statistical Thermodynamics in Chemistry & Biology*. Garland Science, 1st edition, 2002.

[8] S. Gavrilov, M. Vankeerberghen, G. Nelissen, and J. Deconinck. Finite element calculation of crack propagation in type 304 stainless steel in diluted sulphuric acid solutions. *Corrosion Science*, 49(3):980–999, 2007.

[9] T. R. Hendricks and I. Lee. Wrinkle-free nanomechanical film: control and prevention of polymer film buckling. *Nano Letters*, 7(2):372–379, 2007.

[10] C. Herring. Diffusional viscosity of a polycrystalline solid. *Journal of Applied Physics*, 21(5):437 –445, may 1950.

[11] H. Itoh, T. Yamamoto, M. Mori, T. Horita, N. Sakai, H. Yokokawa, and M. Dokiya. Configurational and electrical behavior of ni-ysz cermet with novel microstructure for solid oxide fuel cell anodes. *Journal of the Electrochemical Society*, 144(2):641–646, 1997.

[12] K.E. Thomas-Aleya J. Newman. *Electrochemical Systems*. Prentice-Hall, 3rd edition, 2004.

[13] Q. Jiang, L. H. Liang, and D. S. Zhao. Lattice contraction and surface stress of fcc nanocrystals. *The Journal of Physical Chemistry B*, 105(27):6275–6277, 2001.

[14] A.K.N. Reddy J.O.M. Bockris. *Modern Electrochemistry 2A: Fundamentals of Electrodics*. Springer, 2nd edition, 2001.

[15] D.A. Jones. *Principles and prevention of corrosion*. Prentice Hall, 2nd edition, 1996.

[16] M. Kardar. *Statistical Physics of Particles*. Cambridge University Press, 1st edition, 2007.

[17] J. G. Kirkwood and F. P. Buff. The statistical mechanical theory of surface tension. *Journal of Chemical Physics*, 17:338, 1949.

[18] J. Liang and Z. Suo. Stress-assisted reaction at a solid-fluid interface. *Interface Science*, 9(1):93–104, 2001.

[19] Xiaodong Liu and G.S. Frankel. Effects of compressive stress on localized corrosion in aa2024-t3. *Corrosion Science*, 48(10):3309 – 3329, 2006.

[20] Xiaodong Liu, G.S. Frankel, B. Zoofan, and S.I. Rokhlin. Effect of applied tensile stress on intergranular corrosion of aa2024-t3. *Corrosion Science*, 46(2):405 – 425, 2004.

[21] P. Shrotriya, S. M. Allameh, and W. O. Soboyejo. On the evolution of surface morphology of polysilicon mems structures during fatigue. *Mechanics of Materials*, 36(1):35–44, 2004.

[22] B. J. Spencer, P. W. Voorhees, and S. H. Davis. Morphological instability in epitaxially strained dislocation-free solid films. *Physical Review Letters*, 67(26):3696–3699, 1991.

[23] D.J. Srolovitz. On the stability of surfaces of stressed solids. *Acta Metallurgica*, 37(2):621 – 625, 1989.

[24] R. C. Tolman. The effect of droplet size on surface tension. *Journal of Chemical Physics*, 17:333, 1949.

[25] Chien H. Wu. The chemical potential for stress-driven surface diffusion. *Journal of the Mechanics and Physics of Solids*, 44(12):2059 – 2077, 1996.

[26] Q. Xie, A. Madhukar, P. Chen, and N. P. Kobayashi. Vertically self-organized inas quantum box islands on gaas (100). *Physical Review Letters*, 75(13):2542–2545, 1995.

[27] W. H. Yang and D. J. Srolovitz. Cracklike surface instabilities in stressed solids. *Physical Review Letters*, 71:1593–1596, Sep 1993.